Confinement effect on electrically induced dynamics of a droplet in shear flow

Somnath Santra,[1] Shubhadeep Mandal,[2] and Suman Chakraborty[1,*]
[1]*Department of Mechanical Engineering, Indian Institute of Technology Kharagpur, Kharagpur, West Bengal-721302, India*
[2]*Max Planck Institute for Dynamics and Self-Organization, Am Faβberg 17, D-37077 Göttingen, Germany*

(Received 21 February 2019; revised manuscript received 4 June 2019; published 3 September 2019)

Deformation and breakup of droplets in confined shear flows have been attracting increasing attention from the research community over the past few years, as attributable to their implications in microfluidics and emulsion processing. Reported results in this regard have demonstrated that the primary effect of confinement happens to be the inception of complex oscillating transients, monotonic variation of droplet deformation, and droplet stabilization against breakup, as attributable to wall-induced distortion of the flow field. In sharp contrast to these reported findings, here, we show that a nonintuitive nonmonotonic droplet deformation may occur in a confined shear flow, under the influence of an external electric field. In addition, we demonstrate that the orientation angle of a droplet may either increase or decrease with the domain confinement under the influence of an electric field, whereas the same trivially decreases with the increase in degree of confinement in the absence of any electrical effects. Unlike the typical oscillatory transients observed in microconfined shear flows, we further bring out the possibility of an electrohydrodynamically induced dampening effect in the oscillation characteristics, as governed by a specific regime of the relevant dimensionless electrical parameters. Our results reveal that instead of arresting droplet deformation, the unique hydrodynamics of microconfined shear flow may augment the tendency of droplet breakup, and is likely to alter the droplet breakup mode from midpoint pinching to edge pinching at high electric field strength. These results may bear far reaching implications in a wide variety of applications ranging from the processing of emulsions to droplet based microfluidic technology.

DOI: 10.1103/PhysRevE.100.033101

I. INTRODUCTION

Deformation and breakup of droplets in a confined microfluidic environment have emerged to be of growing interest to the research community over the past few years, as attributable to a plethora of critical applications ranging from droplet based microfluidics and oil recovery to emulsion processing [1–5]. Further, with the advent of microfabrication technology, the external electric field has been progressively used as a novel means of manipulating the morphology of liquid droplets [6–8]. Despite such outstanding relevance, the current understanding of the interplay of electric-field- and confinement-induced hydrodynamic interactions on droplet deformation and dynamical evolution is rather limited, so that the design issues concerning the control of morphodynamics of droplets in a confined medium are often addressed on an empirical basis [9].

When a spherical droplet is subjected to background simple shear flow, the droplet experiences mainly two types of stresses: (a) distorting viscous stress that always tries to deform the droplet toward the flow direction; (b) restoring capillary stress that helps the droplet to retain its spherical configuration. The relative strength of viscous stress over capillary stress is denoted by the capillary number (Ca). For lower values of Ca (Ca $\ll$ 1), the droplet deforms into an ellipsoidal shape and the major axis of the ellipsoid aligns with the extension axis. With a rise in Ca, the deformation enhances and the droplet becomes more aligned in the direction of flow. The droplet deforms into nonellipsoidal shapes in the high Ca regime and beyond a critical point the droplet experiences breakup into smaller droplets. In addition to capillary number, the viscosity ratio λ (the ratio of viscosity of the droplet and suspending fluid) of the system also has a significant role in regulating the deformation dynamics of the droplet.

The interest in deformation dynamics of the droplet in shear flow originated from the classical study of Taylor [10] who constructed an analytical solution for the steady state droplet deformation as a function of capillary number and viscosity ratio. After the pioneering work of Taylor [10], several researchers studied the deformation and breakup of the droplets in a weakly confined domain [11–19]. However, there are physical situations in which the droplet length scale turns out to be of comparable order as that of the channel dimension. In such scenarios, along with the capillary number and viscosity ratio, the confinement ratio (the ratio of droplet diameter to channel height) also plays a crucial role in deformation dynamics of the droplet [5,20–25]. Sibillo *et al.* [22] have experimentally shown the effect of domain confinement on deformation and breakup of the droplets in the presence of simple shear flow. They have demonstrated a transient oscillatory dynamics in the morphodynamic evolution of the droplet, which is normally absent in an unconfined domain. Furthermore, they demonstrated that the steady state deformation also increases with the enhancement of degree of confinement. However, possibly the most interesting aspect of the influence of confinement captured by them is that highly elongated droplets that are otherwise unstable in an

*suman@mech.iitkgp.ernet.in

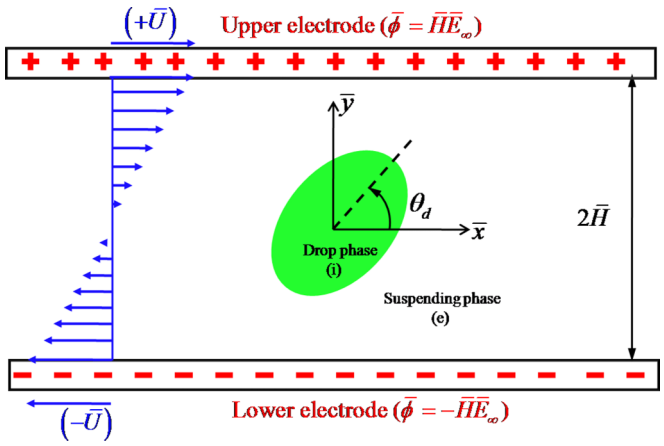

FIG. 1. Schematic illustration of the present problem setup, where a liquid droplet having radius $\bar{a}$ is placed in another liquid medium in a confined domain experiencing both the uniform electric field and simple shear flow. The upper and lower walls move in opposite directions with speed $\bar{U}$. Positive and negative electrodes are attached to the upper and lower walls, respectively. The walls are separated by a distance $2\bar{H}$ and $\bar{E}_\infty$ denotes the magnitude of the imposed electric field. The orientation angle of the droplet between the major semiaxis and the horizontal axis is denoted by θ_d.

unbounded domain may be capable of retaining their equilibrium shape in a confined microenvironment.

With the advent of microelectromechanical systems, electric field has emerged to be a potential governing parameter dictating the dynamical evolution of droplets in a microfluidic environment [26–34]. In a weakly confined domain, a perfect dielectric droplet and a conducting droplet always deform into a prolate configuration (the major axis of the ellipsoidal droplet oriented toward the direction of electric field) [35]. On the other hand, a leaky dielectric droplet (droplet having small but finite electrical conductivity) can deform into an oblate (the major axis of the elliptically deformed droplet oriented perpendicular to the direction of electric field) or prolate configuration depending on the relevant dimensionless electrical properties (conductivity and permittivity ratios) [36].

Here, we bring out unique deformation and breakup dynamics of a leaky and a perfect dielectric droplet in confined shear flow under the action of a transverse uniform electric field. Our investigations exclusively focus on unveiling the interplay of electromechanics- and confinement-induced hydrodynamic interactions toward influencing the following in a manner that is potentially nontrivial as compared to the case of a simple microconfined shear flow: (i) steady state deformation; (ii) transient evolution; (iii) droplet breakup phenomenon.

II. PROBLEM FORMULATION

A. System description

For the present analysis, we have considered a physical system as shown in Fig. 1, where a dielectric liquid droplet is placed in another dielectric fluid medium in a confined domain. The system is subjected to simple shear flow, where the two walls of the domain are moved in opposite directions with speed $\bar{U}$ and a uniform electric field of magnitude $\bar{E}_\infty$ is also applied in the transverse direction. The physical properties of the droplet and the ambient fluid are density ρ_i, ρ_e; the viscosity, μ_i, μ_e; the electric permittivity, ε_i, ε_e; and the electric conductivity, σ_i, σ_e. The surface tension is denoted by Γ. The radius of the undeformed droplet is $\bar{a}$. The subscripts i and e depict the physical parameters at the inside and outside of the droplet, respectively. Due to the application of electric field as well as imposed shear flow, the droplet deforms to a nonspherical shape and the domain confinement also affects the deformation by altering the strength of viscous and electrical stresses. For analyzing the system, a two-dimensional (2D) Cartesian coordinate system has been considered and the origin is fixed at the center of the droplet.

B. Assumptions

For simplifying the present mathematical model, we have considered the following assumptions:

(i) The viscous force and pressure force are more significant as compared to fluid inertia in regulating the flow problem. This necessarily means that the value of the Reynolds number, $\mathrm{Re} = \rho\bar{\dot{\gamma}}\bar{a}^2/\mu_e$ (which stands for the relative strength of inertial stress as compared with viscous stress) is negligible [$\mathrm{Re} \sim O(10^{-4})$].

(ii) The system is neutrally buoyant ($\rho_r = \rho_1/\rho_2 = 1$).

(iii) The effect of charge convection has been neglected which implies that the magnitude of the electric Reynolds number, $\mathrm{Re}_E = \varepsilon_2^2\bar{E}_\infty^2/\mu_2\sigma_2$ (it denotes the relative strength of charge convection over Ohmic conduction) is much smaller than unity.

(iv) For the present leaky dielectric model, the charge relaxation timescale is much smaller as compared to the charge convection timescale (denoted by lower values of Re_E). Thus the charges present at the bulk fluid move to the fluid-fluid interface, relax instantaneously, and the bulk fluids remain charge free. Therefore, we have neglected the effect of transient charging (time derivative of the charge density) [21,37–39].

An example of such a microfluidic system is described as follows: a droplet with radius 4 mm is suspended in another carrier fluid medium in the combined presence of a transverse electric field ($\bar{E}_\infty = 1 \times 10^5$ V/m) and background shear flow. The suspending fluid phase is silicon oil (having $\varepsilon = 2.44 \times 10^{-11}$ F/m, $\sigma = 3.33 \times 10^{-11}$ S/m, $\mu = 12$ Pa s, and $\rho = 980\,\mathrm{kg/m^3}$) and the droplet phase is oxidized castor oil (having $\varepsilon = 10^{-9}$ F/m, $\sigma = 5.57 \times 10^{-11}$ S/m, $\mu = 6.5$ Pa s, and $\rho = 980\,\mathrm{kg/m^3}$). The magnitude of the interfacial tension is 5.5 mN/m. The electrophysical properties of the fluids have been obtained from the experimental analysis of Torza *et al.* [40]. The values of the nondimensional parameters are calculated as $\mathrm{Re}_E \sim O(10^{-2})$, $\mathrm{Re} \sim O(10^{-4})$, and $\rho_r = 1$.

C. Governing equation with phase field method

1. Governing equations for electric potential and the expression of electric force in terms of phase field parameter

In the present analysis, it is assumed that the electric field ($\bar{\mathbf{E}}$) is irrotational ($\bar{\nabla} \times \bar{\mathbf{E}} = 0$) [41]. Therefore, it can be expressed as a gradient in electric potential ($\bar{\phi}$), $\bar{\mathbf{E}} = -\bar{\nabla}\bar{\phi}$.

In the presence of an electric field, the total electric force that acts on a fluid element in a finite domain ($\forall$) is read as

$$\bar{\mathbf{F}}^E = \int_{\forall} (\bar{\nabla}\cdot\bar{\mathbf{T}}^M)d\bar{x}^3, \quad \bar{\nabla}\cdot\bar{\mathbf{T}}^M = q_v\bar{\mathbf{E}} - \frac{1}{2}(\bar{\mathbf{E}}\cdot\bar{\mathbf{E}})\cdot\bar{\nabla}\bar{\varepsilon}. \tag{1}$$

Here $\bar{\mathbf{T}}^M$ and q_v are the Maxwell stress tensor and bulk free charge density, respectively. The first term of the expression of $\bar{\nabla}\cdot\bar{\mathbf{T}}^M$ in Eq. (1) stands for the electric force due to free charges (Coulomb force) and the second term stands for the dielectrophoretic force. In our present study, we have considered two different systems for effective comparison: (a) a leaky dielectric system, where the two interacting fluids (droplet and suspending medium) are leaky dielectric (having small but finite electircal conductivity) in nature, and (b) a perfect dielectric system, where both fluids are perefect dielectric in nature. According to Gauss's law, the volume density of free charges ($\bar{q}_v$) in a dielectric fluid medim of permittivity $\bar{\varepsilon}$ can be expressed as

$$\bar{\nabla}\cdot(\bar{\varepsilon}\bar{\nabla}\bar{\phi}) = \bar{q}_v. \tag{2}$$

In the phase field formalism, $\bar{\varepsilon}$ is expressed as $\bar{\varepsilon} = \frac{1-\varphi}{2}\varepsilon_i + \frac{1+\varphi}{2}\varepsilon_e$, where φ is the phase field parameter. $\varphi = 1$ in the suspending fluid region, whereas $\varphi = -1$ in the inner region of the droplet. The interfacial region is constituted by a diffuse zone, defined by the bounds $-1 < \varphi < 1$. The transient evolution of φ is represented by the Cahn-Hilliard equation:

$$\frac{\partial\varphi}{\partial\bar{t}} + \bar{\mathbf{u}}\cdot\bar{\nabla}\varphi = \bar{\nabla}\cdot(\bar{M}_\varphi\bar{\nabla}\bar{G}), \tag{3}$$

where $\bar{M}_\varphi$ stands for the interface mobility factor. The chemical potential is denoted by $\bar{G} = \Gamma(\varphi^3 - \varphi)/\bar{\zeta} - \Gamma\bar{\zeta}\,\bar{\nabla}^2\varphi$. The thickness of the diffuse interface is regulated by the parameter $\bar{\zeta}$.

For a perfect dielectric sytem, the volume density of free charges is zero. Therefore, the distribution of electric potential is obtained by solving the following govening equation:

$$\bar{\nabla}\cdot(\bar{\varepsilon}\bar{\nabla}\bar{\phi}) = 0. \tag{4}$$

Similarly, for a leaky dielectric system, the distribution of electric potential takes the following form [21,29,42]:

$$\bar{\nabla}\cdot(\bar{\sigma}\bar{\nabla}\bar{\phi}) = 0, \tag{5}$$

where $\bar{\sigma}$ for the two fluid system is expressed as $\bar{\sigma} = \frac{1-\varphi}{2}\sigma_i + \frac{1+\varphi}{2}\sigma_e$ and the electric force on the fluids is calculated by using Eq. (1). On the other hand, for a perfect dielectric system, the electric force on the interacting fluid is simplified to

$$\bar{\mathbf{F}}^E = \int_{\forall}\left[-\frac{1}{2}(\bar{\mathbf{E}}\cdot\bar{\mathbf{E}})\bar{\nabla}\bar{\varepsilon}\right]d\bar{x}^3, \tag{6}$$

where the contribution of free charges on the electric force is dropped out. It is important to mention that the electric potential $\bar{\phi}$ is periodic in the horizontal direction and, at the two walls it satisfies the following boundary condititon:

$$\left.\begin{aligned}\text{upper wall}: \bar{\phi}_e &= \bar{H}\bar{E}_\infty \ \text{ at } \ \bar{y} = \bar{H}\\ \text{lower wall}: \bar{\phi}_e &= -\bar{H}\bar{E}_\infty \ \text{ at } \ \bar{y} = -\bar{H}\end{aligned}\right\}. \tag{7}$$

2. *Coupling between phase field and electrohydrodynamics*

For getting the pressure and velocity field, the continuity equation and the Cahn-Hilliard Navier-Stokes equation have to be solved. It is important to mention that the latter equation couples the phase field formalism with the electrohydrodynamic (EHD). In dimensional form, the continuity equation and Cahn-Hilliard Navier-Stokes equation are expressed as follows:

$$\bar{\nabla}\cdot\bar{\mathbf{u}} = 0, \tag{8}$$

$$\bar{\rho}\left[\frac{\partial\bar{\mathbf{u}}}{\partial\bar{t}} + \bar{\nabla}\cdot(\bar{\mathbf{u}}\bar{\mathbf{u}})\right] = -\bar{\nabla}\bar{p} + \bar{\nabla}\cdot[\bar{\mu}\{\bar{\nabla}\bar{\mathbf{u}} + (\bar{\nabla}\bar{\mathbf{u}}^T)\}] + \bar{G}\bar{\nabla}\varphi + \bar{\mathbf{F}}^E. \tag{9}$$

Here $\bar{\mathbf{F}}^E$ is the electric body force as mentioned in Eqs. (1) and (6) and $\bar{G}\bar{\nabla}\varphi$ denotes the phase field dependent interfacial tension force. Physical properties of fluids μ and ρ are expressed in terms of phase field parameter, which are $\bar{\mu} = \frac{1-\varphi}{2}\mu_i + \frac{1+\varphi}{2}\mu_e$ and $\bar{\rho} = \frac{1-\varphi}{2}\rho_i + \frac{1+\varphi}{2}\rho_e$.The velocity field satisfies the no-slip and no-penetration boundary condition at the two walls that are expressed in the following form ($\mathbf{n_s}$ is the unit normal vector at the solid interface):

$$\left.\begin{aligned}\text{upper wall}: \bar{\mathbf{u}}\cdot\mathbf{n}_s = 0, \quad \bar{\mathbf{u}} - (\bar{\mathbf{u}}\cdot\mathbf{n}_s)\mathbf{n}_s = +\bar{U}\boldsymbol{e_x} \quad \text{at } \bar{y} = \bar{H}\\ \text{lower wall}: \bar{\mathbf{u}}\cdot\mathbf{n}_s = 0, \quad \bar{\mathbf{u}} - (\bar{\mathbf{u}}\cdot\mathbf{n}_s)\mathbf{n}_s = -\bar{U}\boldsymbol{e_x} \quad \text{at } \bar{y} = -\bar{H}\end{aligned}\right\}. \tag{10}$$

where $\boldsymbol{e_x}$ is the unit vector along the x direction. Furthermore, the periodic boundary condition has been used in the horizontal direction for velocity field and pressure fields.

3. *Governing equations in nondimensional format*

To nondimensionalize the governing equation, we have used the following nondimensional scheme: length is nondimensionalized by $\bar{a}$, velocity by $\bar{\dot{\gamma}}\bar{a}$ (where $\bar{\dot{\gamma}}$ is the shear rate), electric field by $\bar{E}_\infty$, electric stress by $\varepsilon_e\bar{E}_\infty^2$, and viscous stress by $\mu_e\bar{\dot{\gamma}}$. From the above nondimensional scheme, we have fixed some nondimensional numbers, which are capillary number $\mathrm{Ca} = \mu_e\bar{\dot{\gamma}}\bar{a}/\Gamma$ (it stands for relative magnitude of viscous over capillary stresses), electric capillary number $\mathrm{Ca}_E = \varepsilon_e\bar{E}_\infty^2\bar{a}/\Gamma$ (which stands for the relative strength of electric stress over capillary stress), Masson number $M = \varepsilon_e\bar{E}_\infty^2/\mu_e\bar{\dot{\gamma}}$ (which symbolizes the relative strength of electric stress over viscous stresses), Reynolds number $\mathrm{Re} = \rho\bar{\dot{\gamma}}\bar{a}^2/\mu_e$, and domain confinement ratio $\mathrm{Wc} = 2\bar{a}/2\bar{H}$ (the ratio of droplet diameter and channel height). Furthermore, we have also identified some nondimensional property ratios: viscosity ratio $\lambda = \mu_i/\mu_e$, permittivity ratio $S = \varepsilon_i/\varepsilon_e$, and conductivity ratio $R = \sigma_i/\sigma_e$. In the nondimensional form, the

Cahn-Hilliard equation can be expressed as

$$\frac{\partial \varphi}{\partial t} + \mathbf{u}\cdot\nabla\varphi = \frac{1}{\mathrm{Pe}}(\nabla^2 G), \quad \text{where}$$
$$G = \frac{1}{\mathrm{Cn}}(\varphi^3 - \varphi) - \mathrm{Cn}\nabla^2\varphi, \tag{11}$$

where $\mathrm{Pe} = (\bar{a}^3\bar{\dot{\gamma}}/\bar{M}_\varphi\,\Gamma)$ denotes the Péclet number and $\mathrm{Cn} = \bar{\xi}/\bar{a}$ denotes the Cahn number. Throughout our numerical analysis, we have used a very high value of Péclet number ($\mathrm{Pe} = 1800$) [43]. The Péclet number independence test is given in Appendix D. For obtaining the electric potential, we have to solve the following governing equation:

$$\left.\begin{aligned}&\text{Leaky dielectric system}: \ \nabla\cdot(\sigma\nabla\phi) = 0\\ &\text{Perfect dielectric system}: \ \nabla\cdot(\varepsilon\nabla\phi) = 0\end{aligned}\right\}. \tag{12}$$

Similarly, Eqs. (8) and (9) are represented in the following format:

$$\nabla\cdot\mathbf{u} = 0, \tag{13}$$

$$\mathrm{Re}\left[\frac{\partial \mathbf{u}}{\partial t} + \nabla\cdot(\mathbf{uu})\right] = -\nabla p + \nabla\cdot[\mu\{\nabla\mathbf{u} + (\nabla\mathbf{u})^T\}] + \frac{1}{\mathrm{Ca}}G\nabla\varphi + M\mathbf{F}^E. \tag{14}$$

In the paradigm of the phase field formalism, the fluid properties are characterized in the following manner:

$$\left.\begin{aligned}\rho &= \tfrac{(1-\varphi)}{2}\rho_r + \tfrac{(1+\varphi)}{2}, \quad \mu = \tfrac{(1-\varphi)}{2}\lambda + \tfrac{(1+\varphi)}{2}\\ \varepsilon &= \tfrac{(1-\varphi)}{2}S + \tfrac{(1+\varphi)}{2}, \quad \sigma = \tfrac{(1-\varphi)}{2}R + \tfrac{(1+\varphi)}{2}\end{aligned}\right\}. \tag{15}$$

For solving the governing equations (11)–(14), we have used finite element solver COMSOL MULTIPHYSICS.

III. RESULTS AND DISCUSSIONS

A. Comparison between the numerical and analytical results

First of all, we compare the numerical result with the analytical solution. The analytical solution is developed in an unbounded domain by the implementation of the regular perturbation method considering Ca as a perturbation variable (shown in Appendix A). In the regular perturbation method, the expansion of the droplet radius in asymptotic form can be represented in the following shape [44,45]:

$$r_s = 1 + f(\theta) = 1 + \mathrm{Ca}f^{(Ca)} + \mathrm{Ca}^2 f^{(Ca^2)} + O(\mathrm{Ca}^3). \tag{16}$$

In Eq. (16), $f^{(\mathrm{Ca})}$ and $f^{(\mathrm{Ca}^2)}$ show the deviation in droplet shape under the deformed condition and express it as

$$f^{(\mathrm{Ca})} = \left[L_{2,0}^{(\mathrm{Ca})}\cos(2\theta) + \hat{L}_{2,0}^{(\mathrm{Ca})}\sin(2\theta)\right],$$
$$f^{(\mathrm{Ca}^2)} = L_{0,1}^{(\mathrm{Ca}^2)} + \begin{bmatrix} L_{2,1}^{(\mathrm{Ca}^2)}\cos(2\theta) + \hat{L}_{2,1}^{(\mathrm{Ca}^2)}\sin(2\theta) + L_{3,1}^{(\mathrm{Ca}^2)}\cos(3\theta) \\ +\hat{L}_{3,1}^{(\mathrm{Ca}^2)}\sin(3\theta) + L_{4,1}^{(\mathrm{Ca}^2)}\cos(4\theta) + \hat{L}_{4,1}^{(\mathrm{Ca}^2)}\sin(4\theta)\end{bmatrix}. \tag{17}$$

Here θ is the polar angle. The expression of $L_{2,0}^{(\mathrm{Ca})}$ and $\hat{L}_{2,0}^{(\mathrm{Ca})}$ have been obtained as

$$L_{2,0}^{(\mathrm{Ca})} = -\frac{1}{3}M\frac{\Phi}{(R+1)^2}(1 - \mathrm{e}^{-\frac{t}{\lambda+1}}), \quad \hat{L}_{2,0}^{(\mathrm{Ca})} = (1 - e^{-\frac{t}{\lambda+1}}). \tag{18}$$

The pattern of interface deformation due to the sole effect of electric field depends on Φ, expressed as $\Phi = R^2 + R - 3S + 1$ [41]. The electric field will deform the droplet into a prolate (or oblate) shape for $\Phi > 0$ (or $\Phi < 0$). The degree of droplet deformation is measured by deformation parameter D and is expressed as

$$D = \frac{\max r_s(\theta) - \min r_s(\theta)}{\max r_s(\theta) + \min r_s(\theta)}. \tag{19}$$

For a highly deformed droplet, when the droplet is no longer elliptical, the deformation of the droplet is quantified through the following expression:

$$L = \max r_s(\theta). \tag{20}$$

Another important parameter related to droplet shape is the droplet orientation angle (θ_d) that is formed by the major axis of the elliptical droplet with the direction of shear flow. A simple mathematical expression of θ_d is

$$\theta_d = \frac{1}{2}\tan^{-1}\left(\frac{L_{2,0}^{(\mathrm{Ca})}}{\hat{L}_{2,0}^{(\mathrm{Ca})}}\right), \tag{21}$$

where $O(\mathrm{Ca})$ deformation has been taken into consideration. The droplet orientation angle considering $O(\mathrm{Ca}^2)$ deformation is obtained numerically.

For examining the effect of different governing parameters on steady and transient deformation characteristics of the droplet, both the perfect dielectric system (PD-PD system considering both $S > 1$ and $S < 1$) and the leaky dielectric system (LD-LD system considering both $\Phi > 0$ as well as $\Phi < 0$) have been taken into consideration. The grid independence study of the numerical simulation is shown in Appendix B. For checking the applicability of the present numerical result, we also validated our numerical result with the experimental results of Sibillo *et al.* [22], Tsukada *et al.* [46], and Salipante and Vlahovska [47]. The details of the analysis are shown in Appendix C. Furthermore, for confirming the accuracy of the present numerical results, we have performed a comparison between the analytical results and the result obtained from numerical simulations. At first, we compare the steady state deformation parameters of the droplet for different capillary numbers. Through numerical simulations, we have also inferred that the presence of the wall has negligible impact on the deformation of the droplet for $\mathrm{Wc} \leqslant 0.2$. Thus,

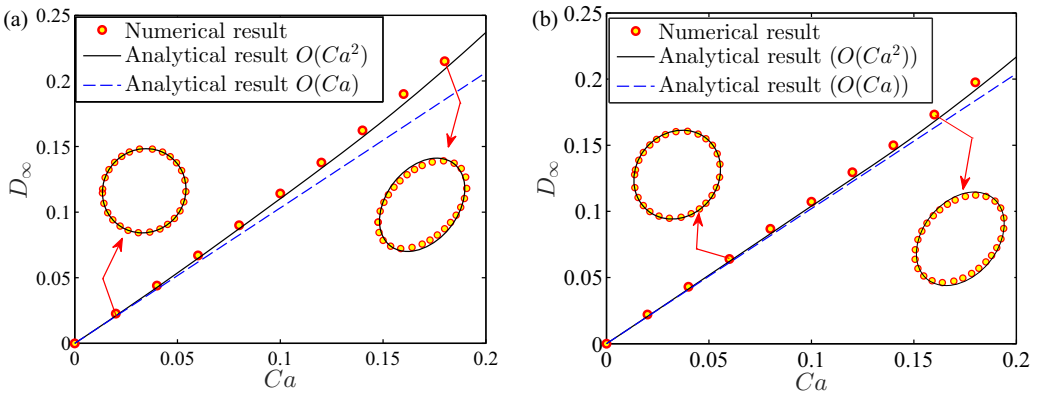

FIG. 2. Variation of D_∞ with Ca for (a) a PD-PD system with $S = 15$, (b) a LD-LD system with $(R, S) = (2, 0.5)$. Others parameters are $M = 1$, $\lambda = 1$, Wc $= 0.2$, and Re $= 0.01$.

we compare the analytical solution (neglecting the presence of the wall) with the numerical solution obtained at Wc $= 0.2$. Figure 2(a) depicts the alteration of D_∞ with Ca for PD-PD system with $S = 15$. Similarly, Fig. 2(b) shows the alteration of steady state droplet deformation (D_∞) with Ca for the LD-LD system with $(R, S) = (2, 0.5)$. It is apparent from Fig. 2 that the analytical solution [leading-order linear theory corrected up to O(Ca) as well as the higher-order nonlinear theory corrected up to $O(\text{Ca}^2)$] and the numerical solution show good agreement with each other for lower values of Ca. However, the higher-order nonlinear theory offers better prediction of the numerical results than the leading-order linear theory for comparatively higher value of Ca.

B. Domain confinement-induced alteration of steady state deformation

1. Perfect dielectric systems

Figures 3(a) and 3(b) illustrate the variation of steady state deformation parameter (D_∞) and orientation angle $(\theta_{d,\infty})$ of the droplet with domain confinement for a PD-PD system having $S = 2$. We have the varied confinement ratio (Wc) from 0.2 (unbounded domain) to 0.8 (extremely confined domain) by altering the height of the computational domain, keeping other parameters intact. Figure 3(a) shows that the steady state value of the deformation parameter enhances with the enhancement of domain confinement in the absence of an electric field. This finding has been mentioned in the experimental observation of Sibillo *et al.* [22]. However, this behavior is dramatically altered in the presence of an electric field. In an electrohydrodynamic system, the value of D_∞ decreases with Wc up to Wc ≈ 0.30 and, above it, the magnitude of D_∞ again increases with Wc. Figure 3(b) shows that the orientation angle of the droplet is higher for the electrified system compared to the nonelectrified case in a weakly confined domain. However, the orientation angle of the droplet for both cases (electrified and nonelectrified) decreases monotonically with the domain confinement. These observations are valid for any PD-PD system having $S > 1$.

Before discussing the physical explanation behind the above observed phenomenon, it is imperative to discuss different forces that cause the deformation of the droplet. In the sole presence of background shear flow, the deformation of the droplet is caused by flow-induced viscous stress and its magnitude increases with the enhancement of channel confinement. On the other side, when a leaky dielectric droplet, suspended in a leaky dielectric medium, is exposed to uniform electric field, the fluids get polarized and the free charges are instantaneously moved to the interface [41]. In the presence of an electric field, the action of both the tangential and normal

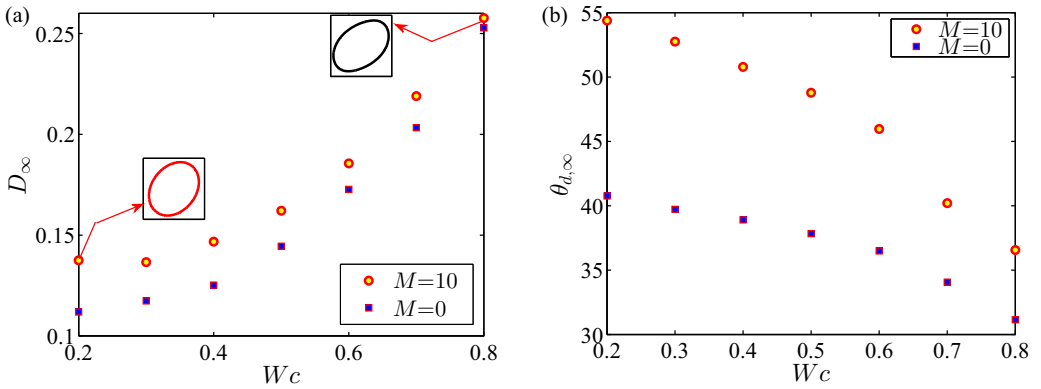

FIG. 3. Effect of confinement on the (a) D_∞, (b) $\theta_{d,\infty}$ of a PD-PD system with $S = 2$. Others parameters are Ca $= 0.1$, $\lambda = 1$, and Re $= 0.01$.

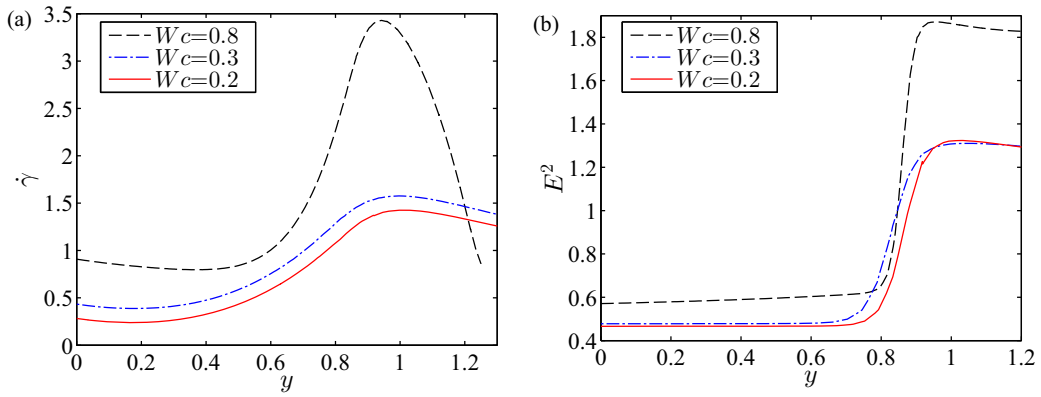

FIG. 4. Variation of (a) shear rate, (b) E^2 with the vertical distance at the tip of the droplet ($x = 0.85$) for a PD-PD system with $S = 2$. Other parameters are Re $= 0.01$, $\lambda = 1$, and $M = 10$.

components of electric field on the free charges generates electric stress at the interface. Both the tangential and normal components of the electric stresses are discontinuous across the interface except for a few special cases. The imbalance in the normal component of electric stress or the net normal electric stress directly participates in the deformation of the droplets. On the other hand, the imbalance in tangential electric stress leads to a net hydrodynamic shear stress and creates fluid flow circulation in and around the droplet in order to balance the tangential component of hydrodynamic stress at the interface. The normal component of hydrodynamic stress, termed "normal hydrodynamic stress," originates from the fluid flow and plays a prime role in setting the interface deformation. Based on leading-order asymptotic analysis, Behjatian and Esmaeeli [48] have obtained the following form of the normal hydrodynamic stress in a confined domain:

$$\tau_h^n = C^2 F \frac{\varepsilon_o E_\infty^2 (R-S)}{(R+1)^2} \sin(2\theta), \tag{22}$$

where θ is the polar angle. C and F have appeared due to the presence of a confined wall and are expressed as $C = \frac{R+1}{(R+1)-\mathrm{Wc}^2(R-1)}$, $F = \frac{(\mathrm{Wc}^2-1)^2\lambda-(\mathrm{Wc}^4+6\mathrm{Wc}^2-1)}{(\mathrm{Wc}^2-1)^2\lambda+(1-\mathrm{Wc}^4)}$. In the expressions of C and F, Wc denotes the confinement ratio.

For a perfect dielectric system, the net tangential electric stress acting at the interface is zero, since the free charge present at the interface is zero (the fluids have no free electron at the outermost atomic shell). Due to that reason, there is no fluid flow circulation in and around the droplet. Thus, there is no normal hydrodynamic stress. For a perfect dielectric system, the presence of the electric field polarizes fluids. The polarization creates dipole moments which align themselves in the direction of the electric field and generates polarization stress (also called normal electric stress), which always acts normal to the interface and is directed from the fluid having higher electrical permittivity to lower electrical permittivity.

It was previously mentioned that, in the sole presence of background shear flow, the deformation of the droplet is caused by flow-induced viscous stress and its magnitude increases with the enhancement of the degree of domain confinement. Therefore, the deformation also increases. However, in the presence of an electric field, one additional electric normal stress also acts as mentioned earlier and the deformation phenomenon relies on the interplay between normal electric stress and viscous stress. It is worth mentioning that the strength of the normal electric stress depends on electric field strength as well as domain confinement, whereas viscous stress is only governed by the domain confinement for a given shear flow [20,22]. Another important fact is that the normal electric stress always tries to deform the droplet into a prolate configuration whereas viscous stress tries to deform it along the direction of flow and reduces the effect of normal electric stress.

In Figs. 4(a) and 4(b), we have shown the variation of nondimensional shear rate ($\dot{\gamma}$) and the square of nondimensional electric field strength (E^2) with domain confinements at the droplet tip, respectively. Shear rate measures the strength of viscous drag, whereas the square of the electric field strength measures the strength of normal electric stress. From the figure, we obtain that in an unbounded domain, the normal electric stress is dominating as the strength of viscous stress is low (as the average magnitude of E^2 is more than $\dot{\gamma}$). Hence, the orientation angle of the droplet is more and the droplet aligns more toward the electrode. The figures also reveal that both entities increase notably with domain confinement. However, the enhancement of viscous stress is much higher as compared to the normal electric stress for the considered value of S. This can be confirmed from the droplet shape in Fig. 3(a), where it is obtained that the droplet is aligned more in the direction of flow in a highly confined domain. This is only possible when the enhancement of viscous stress is more compared to normal electric stress. This viscous stress tries to reduce the deformation and orientation angle via retarding the effect of normal electric stress and the net effect is minimum at Wc $= 0.3$. Therefore, the deformation parameter achieves its minimum value at Wc $= 0.3$. After Wc $= 0.3$, the viscous stress becomes dominating. Hence, in this regime, the deformation of the droplet increases with Wc due to the enhancement of viscous stress and the orientation angle of the droplet decreases.

Figures 5(a) and 5(b) show a similar variation in deformation characteristic and orientation angle for a PD-PD system having $S = 0.1$ (the same is valid for $S < 1$). For this system, in the presence of an electric field, the magnitude of D_∞ decreases until the confinement ratio approaches 0.5 and, above it, further increase in domain confinement results in the

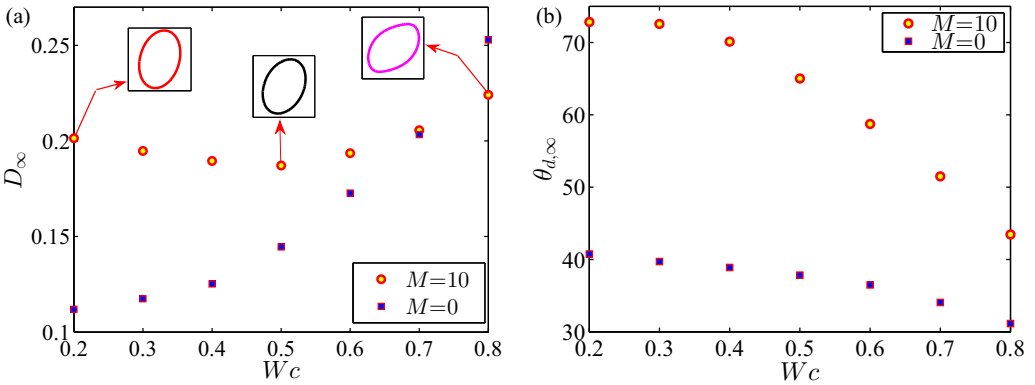

FIG. 5. Effect of confinement on the (a) D_∞, (b) $\theta_{d,\infty}$ of a PD-PD system with $S = 0.1$. Others parameters are Ca $= 0.1$, $\lambda = 1$, and Re $= 0.01$.

enhancement of the deformation parameter. From Fig. 5(b), it is also observed that orientation angles for both the electrified and nonelectrified case decrease with the enhancement of domain confinement similar to the PD-PD system with $S = 2$ ($S > 1$). Like the previous PD-PD system ($S > 1$), a similar interplay between normal electric stress and viscous stress is responsible for the observed variation in deformation characteristic and orientation angle of the present perfect dielectric droplet.

2. *Leaky dielectric systems*

Figures 6(a) and 6(b) show the variation of steady state deformation and orientation angle with domain confinement for the LD-LD system having (R, S) = (2, 0.5). From Fig. 6(a), another remarkable change is observed in the deformation characteristic in the presence of an electric field, where the droplet deformation reduces with increase in the domain confinement and in a weakly confined domain (Wc < 0.3), it experiences the breakup phenomenon. On the other hand, the orientation angle of the droplet both for an electrified and a nonelectrified system decreases with domain confinement. However, the orientation angle is much higher in the electrified case as compared to the nonelectrified case.

Here, we have provided the physical reason behind the above observed behavior. For the leaky dielectric model, in addition to normal electric stress and viscous stress, the normal hydrodynamic stress also acts. The normal hydrodynamic stress is generated from the fluid flow in and around the droplet caused by the mismatch in the tangential electric stress. In an unbounded domain, the directions of both the normal electric and hydrodynamic stress are the same. However, the latter one shows interesting behavior in the confined domain, where its magnitude decreases with increase in the domain confinement and beyond a particular domain confinement ratio, its direction becomes opposite [21,48]. In this regime, it tries to reduce the effect of normal electric stress. For the present LD-LD system, at lower domain confinement, both the normal electric and hydrodynamic stresses act in the direction of electric field and attempt to deform the droplet into a prolate shape. This occurs because of the positive value of the deformation characteristic function ($\Phi > 0$). On the other hand, the viscous stress tries to deform it along the flow direction though its magnitude is small due to low confinement. In the presence of higher electric field strength ($M = 20$), the combined strength of normal electric and hydrodynamic stress is more in a weakly confined domain that creates higher deformation as well as the orientation angle of the droplet. With the enhancement of domain confinement, both normal electric stress and viscous stress increase similar to the

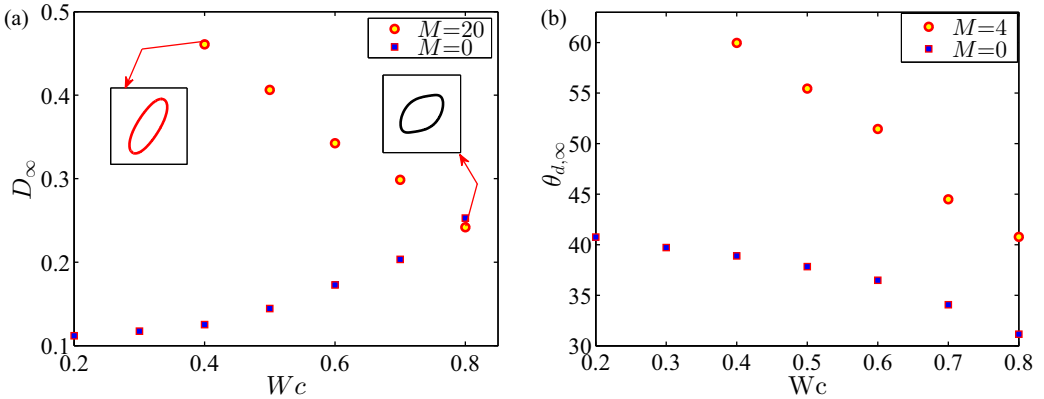

FIG. 6. Effect of confinement on the (a) D_∞, (b) $\theta_{d,\infty}$ of a LD-LD system with (R, S) = (2, 0.5). Other parameters are Ca $= 0.1$, $\lambda = 1$, and Re $= 0.01$.

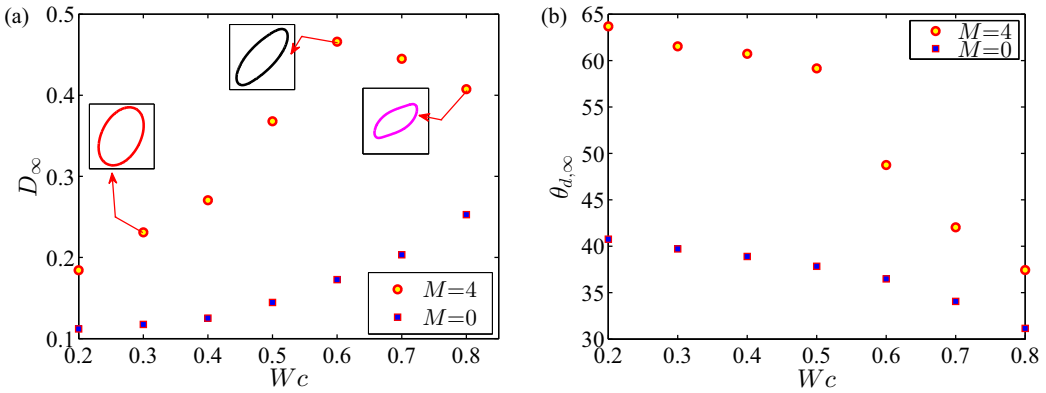

FIG. 7. Effect of confinement on the (a) D_∞, (b) $\theta_{d,\infty}$ of a LD-LD system with $(R, S) = (10, 1)$. Other parameters are Ca $= 0.1$, $\lambda = 1$, and Re $= 0.01$.

PD-PD system as depicted in Figs. 4(a) and 4(b), whereas the magnitude of normal hydrodynamic stress decreases. After a certain confinement ratio (for the present case, Wc ≈ 0.5), it becomes reversed and acts in the direction of viscous stress. Thus, in a confined domain, the strength of normal electric stress is reduced by the integrated effect of viscous stress and reversed normal hydrodynamic stress. Hence, the reduction in the deformation as well as the orientation angle of the droplet is observed.

Figures 7(a) and 7(b) depict the evolution of the steady state deformation parameter and orientation angle for the LD-LD system having $(R, S) = (10, 1)$. For the present system, one must acknowledge that the conductivity ratio is much higher than the permittivity ratio ($R \gg S$) unlike the previous LD-LD system. Because of that, in the presence of an electric field, a significant alteration is observed in the deformation characteristic, where the deformation increases with Wc until the domain confinement reaches 0.6, and additional increase in Wc creates reduction in the deformation as depicted in Fig. 7(a). On the other hand, Fig. 7(b) shows that orientation angle decreases monotonically with domain confinement.

The physical interpretation of the above observed phenomenon is now provided. For the considered leaky dielectric system, normal electric stress and hydrodynamic stress try to deform the droplet toward the electrode in the unbounded domain. This is due to the positive value of the deformation characteristic function ($\Phi > 0$). On the contrary, the viscous stress tries to deform it toward the flow direction though its strength is less compared to the former two stresses. Therefore, the orientation angle of the droplet is more in a weakly confined domain. With increase in the Wc, the strength of normal electric stress and viscous stress increases, whereas normal hydrodynamic stress decreases. Such enhancement of viscous stress and reduction of normal hydrodynamic stress are the main reasons behind the reduction of orientation angle with domain confinement. For the present case, as the liquid droplet is more conducting than the ambient fluid ($R = 10$), the strength of normal electric stress is significantly high in the confined domain. Hence, the deformation increases with Wc up to Wc $= 0.6$ due to the dominating role of normal electric stress. However, after Wc $= 0.6$, the integrated effect of reversed normal hydrodynamic stress and viscous stress becomes dominating, which lowers the deformation by diminishing the effect of normal electric stress and reduces the orientation angle by aligning the droplet more toward the flow direction.

Figures 8(a) and 8(b) show the variation of deformation parameter with confinement ratio for a leaky dielectric system having $(R, S) = (0.033, 0.4397)$. For the present system, Fig. 8(a) shows another striking change in the deformation characteristic in the presence of an electric field, where the steady state deformation value decreases with Wc up to

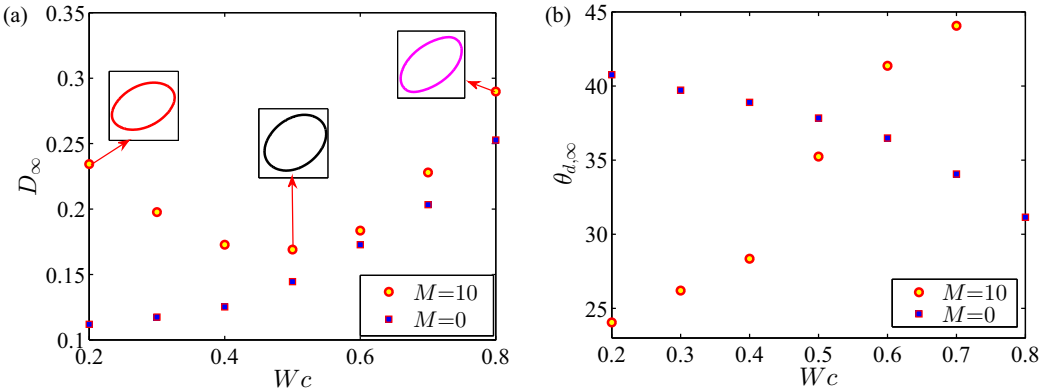

FIG. 8. Effect of confinement on the (a) D_∞, (b) $\theta_{d,\infty}$ of a LD-LD system with $(R, S) = (0.033, 0.4397)$. Others parameters are Ca $= 0.1$, $\lambda = 1$, and Re $= 0.01$.

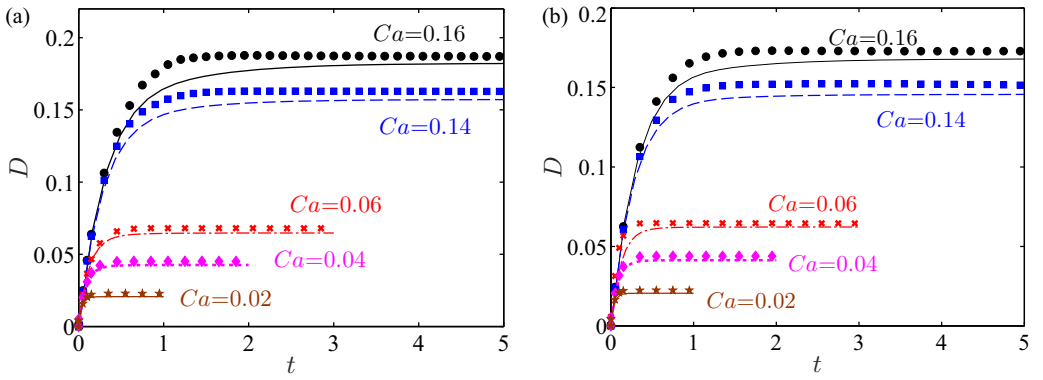

FIG. 9. Transient variation of deformation parameter (a) a PD-PD system with $S = 15$, (b) a LD-LD system with $(R, S) = (2, 0.5)$. Others parameters are $M = 1$, $\lambda = 1$, Wc $= 0.2$, and Re $= 0.01$.

Wc ≈ 0.5 and additional increase in Wc again enhances the deformation. Another remarkable aspect of domain confinement in the presence of an electric field is reflected in Fig. 8(b), where the orientation angle of the droplet increases with domain confinement unlike the nonelectrified system.

The reason behind the observed droplet deformation phenomenon is now presented. In the unbounded domain, for the present leaky dielectric system, the normal electric stress and normal hydrodynamic stress attempt to deform the droplet along the flow direction similar to viscous stress. This happens due to the negative values of deformation characteristic function ($\Phi < 0$), where the electric field induces an oblate deformation in droplet shape. In the presence of electric field strength, their united strength is high, which causes higher deformation and aligns the droplet toward the flow direction. Hence the orientation angle is small. However, with increase in the domain confinement, the normal hydrodynamic stress reduces significantly. Because of that, the steady state deformation reduces and the orientation angle increases. At Wc ≈ 0.5, the normal hydrodynamic stress becomes reversed. Therefore, the deformation is minimum. For additional increment in Wc above 0.5, the magnitude of reversed normal hydrodynamic stress increases, which enhances the deformation of the droplet and tries to align the droplet toward the electrode. Due to that reason, the orientation angle is maximum in a confined domain.

C. Domain confinement-induced alteration in transient droplet deformation characteristics

Figure 9 depicts the transient evolution of the deformation parameter for different values of Ca. We have shown both the analytical result obtained from higher-order nonlinear theory corrected up to $O(\mathrm{Ca}^2)$ (shown by line) and the numerical result (shown by markers), and performed a comparison between them. The variation of D with time for a PD-PD system having $S = 15$ has been shown in Fig. 9(a), whereas Fig. 9(b) shows the variation for the LD-LD system having $(R, S) = (2, 0.5)$. From the figures, it is understood that the analytical result shows good agreement with the numerical result for smaller values of Ca. However, at larger values of Ca, the deviation is seen to be higher for all the systems.

Next, we have analyzed the transient droplet deformation characteristic in a confined domain under different electric field strengths. For that, we have varied the Masson number by changing the values of Ca_E while keeping the value of Ca unaltered. First, we have shown the result for PD-PD systems and, subsequently, the results have been shown for LD-LD systems.

1. Perfect dielectric systems

Figures 10(a) and 10(b) show the transient variation of the deformation parameter (L) and orientation angle (θ_d),

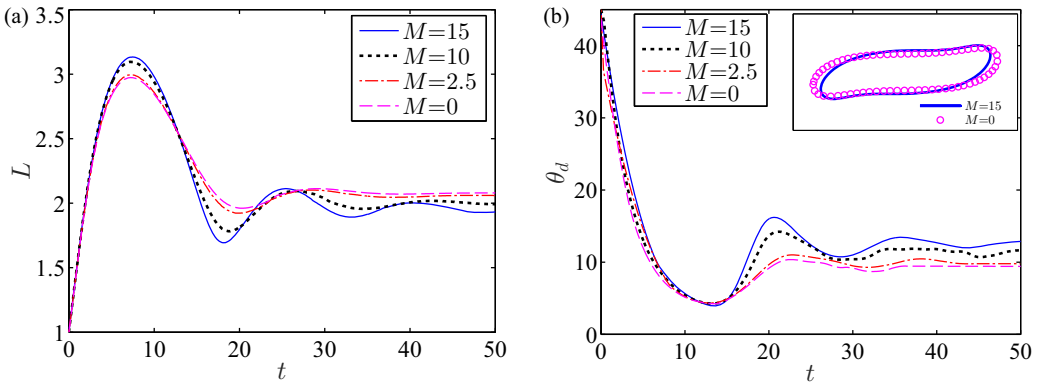

FIG. 10. Variation of (a) L and (b) θ_d with t for a PD-PD system with $S = 2$. Other parameters are Ca $= 0.4$, $\lambda = 1$, Re $= 0.01$, and Wc $= 0.909$. The inset shows the contours of the droplet at steady state for $M = 0$ and $M = 15$.

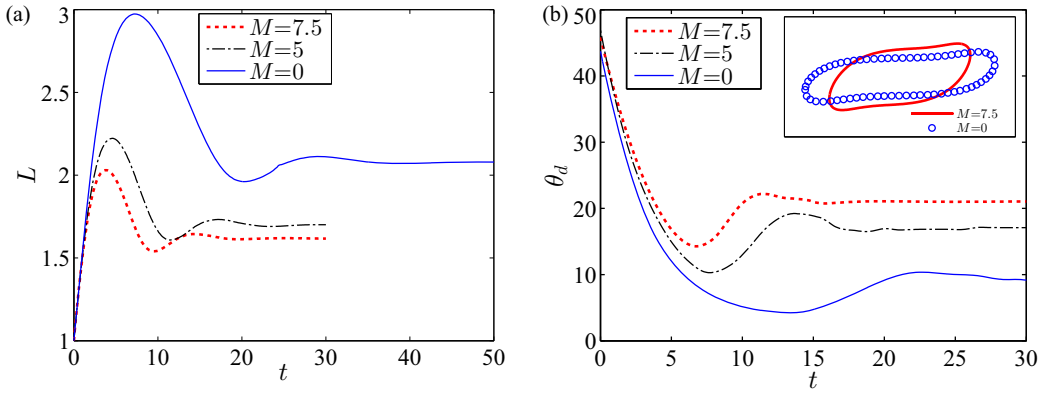

FIG. 11. Variation of (a) L and (b) θ_d with t for a PD-PD system with $S = 0.1$. Other parameters are Ca $= 0.4$, $\lambda = 1$, Re $= 0.01$, and Wc $= 0.909$. The inset shows the contour of the droplet at steady state for $M = 0$ and $M = 7.5$

respectively, for the PD-PD system with $S = 2$ for different values of M. It is observed that, in the absence of an electric field ($M = 0$), the droplet deformation experiences maxima and minima in a damped oscillatory manner as previously reported by Sibillo *et al.* [22]. However, a striking difference is observed in the deformation characteristic due to the application of an electric field, where the presence of an electric field induces additional oscillation in the deformation and orientation of the droplet and the unsteadiness increases with increase in the value of M. Therefore the time required to reach the steady state configuration, termed "steady state time," also increases. On the other hand, from Fig. 10(a), it is also obtained that the steady state deformation value reduces with increase in the value of M ($L_\infty = 1.992$ for $M = 5$ and $L_\infty = 2.07$ for $M = 0$). This observation is valid for any PD-PD system having $S > 1$.

Figures 11(a) and 11(b) depict the variation of L and θ_d with time, respectively, for a PD-PD system with $S = 0.1$. For $S = 0.1$(the same is applicable for $S < 1$), Fig. 11(a) reveals that the presence of an electric field reduces the value of steady state deformation and it becomes lower with increase in the value of M ($L_\infty = 1.617$ for $M = 7.5$ and $L_\infty = 2.07$ for $M = 0$), like $S = 2$. But the interesting fact is that the oscillation observed in deformation and orientation in the absence of an electric field ($M = 0$) gradually diminishes as we increase electric field strength.

For the perfect dielectric systems in the presence of an electric field, it is well established that the deformation of droplet interface is governed by the normal electric stress due to the electric field and the viscous stress due to the shear flow. For a higher value of Ca (here Ca $= 0.4$) and Wc, the viscous stress is significant and attempts to deform the droplet along its direction. On the other hand, the electric normal stress tries to deform it in the prolate shape that is perpendicular to the shear plane. For both systems, in the absence of an electric field, the viscous stress is higher due to higher values of Ca, and it regulates the droplet deformation phenomenon. In the presence of an electric field, the normal electric stress comes into play. As we increase the value M (or Ca_E), the normal electric stress increases which reduces the deformation via lowering the effect of viscous stress, and it tries to deform the droplet along its direction. Therefore, the droplets are aligned more in the direction of the electrode as shown in Figs. 10(b) and 11(b). The unsteadiness in the deformation behavior occurs due to continuous elongation and relaxation of the droplet interface. It is necessary to state that this elongation and relaxation are coupled with forward and backward rotation of the droplet that is again governed by the normal electric force, viscous stress force, and surface tension force on the droplet. The interplay among these forces finally determines the time at which the droplet achieves steady state configuration.

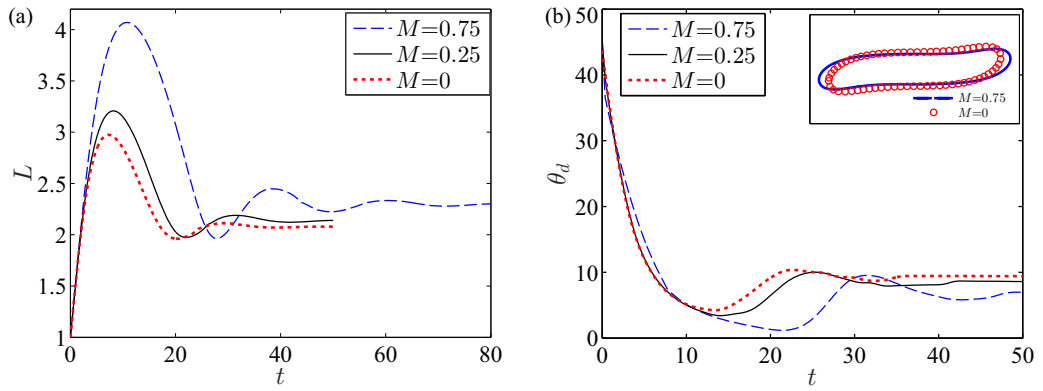

FIG. 12. Variation of (a) L and (b) θ_d with t for a LD-LD system with $(R, S) = (0.5, 2)$. Other parameters are Ca $= 0.4$, $\lambda = 1$, Re $= 0.01$, and Wc $= 0.909$. The inset shows the contour of the droplet at steady state for $M = 0$ and $M = 0.75$.

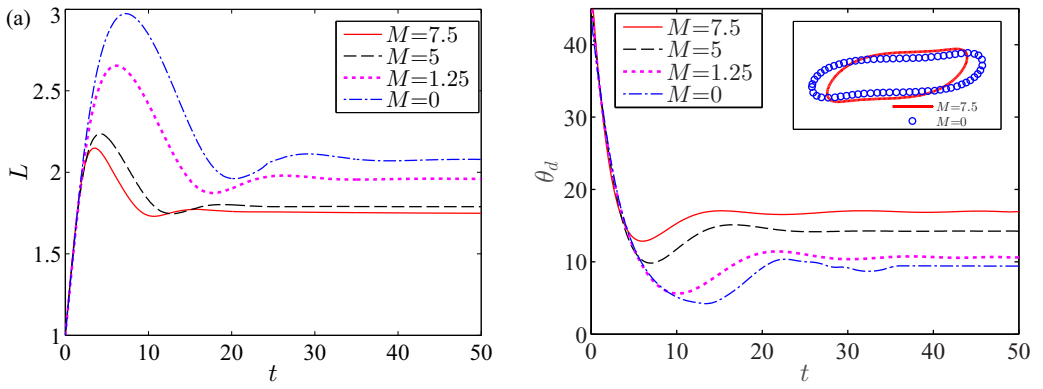

FIG. 13. Variation of (a) L and (b) θ_d with t for LD-LD system with $(R, S) = (2, 0.5)$. Other parameters are Ca $= 0.4$, $\lambda = 1$, Re $= 0.01$, and Wc $= 0.909$. The inset shows the contour of the droplet at steady state for $M = 0$ and $M = 7.5$.

2. Leaky dielectric systems

Figures 12(a) and 12(b) depict the transient evolution of L and θ_d, respectively, for the LD-LD system with $(R, S) = (0.5, 2)$. From both figures, it is understood that the presence of an electric field creates extra oscillation in the deformation and orientation of the droplet and the unevenness in the transient deformation characteristic increases with M which creates a higher steady state time. Along with steady state time, the steady state deformation also increases with increase in the value of M ($L_\infty = 2.07$ for $M = 0$ and $L_\infty = 2.301$, $M = 0.75$).

This deformation dynamics can be explained by considering the effect of normal hydrodynamic stress along with normal electric stress and viscous stress. For the considered values of (R, S), the combined action of viscous stress and normal electric stress tries to deform the droplet into an oblate shape (along the flow direction) whereas the hydrodynamic normal stress tries to deform it into a prolate shape due to the reversal of its direction in the confined domain. With increase in the value of M, the combined magnitude of viscous stress and electric normal stress has been increased which ultimately increases the value of L and tries to align the droplet along the flow direction as shown in Fig. 12(b). For the present case, as deformation increases with M, the interface deforms more for locally balancing the stresses which increases the time to achieve steady state configuration.

Similarly, Figs. 13(a) and 13(b) also illustrate the transient variation of L and θ_d, respectively, for different values of M for the LD-LD system with $(R, S) = (2, 0.5)$. For the present case, the presence of an electric field suppresses the oscillation in the deformation and orientation of the droplet unlike the LD-LD system having $\Phi < 0$. Therefore, the steady state time decreases with increase in M. Furthermore, the value of the deformation parameter also decreases with increase in M ($L_\infty = 1.749$ for $M = 7.5$ and $L_\infty = 2.07$ for $M = 0$) as shown in Fig. 13(a).

For the considered value of the permittivity and conductivity ratio, the magnitude of normal electric stress is much higher (as it is quadratic in R) than the normal hydrodynamic stress which acts in the opposite direction of normal electric stress. Therefore, the net normal stress tries to deform the droplet along the vertical direction (prolate shape), whereas the viscous stress tries to deform it along the direction of flow. In the absence of an electric field ($M = 0$), the higher viscous stress creates a large droplet deformation along the flow direction at a higher value of Ca. As M increases, the net normal stress also increases which lowers the deformation parameter via reducing the effect of viscous stress and tries to align the droplet along the vertical direction as shown in Fig. 13(b). For

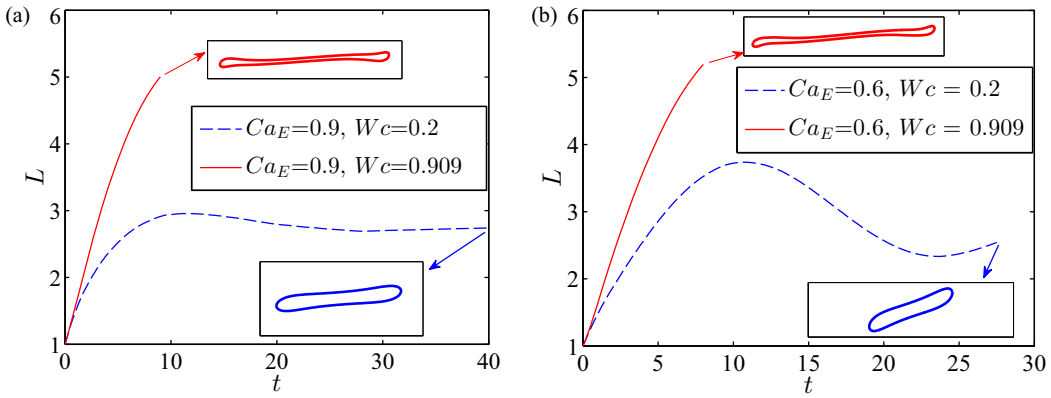

FIG. 14. Effect of confinement on droplet breakup for (a) a PD-PD system with $S = 15$ and (b) a LD-LD system with $(R, S) = (0.5, 2)$. Other parameters are Re $= 0.01$, $\lambda = 1$, and $M = 1$.

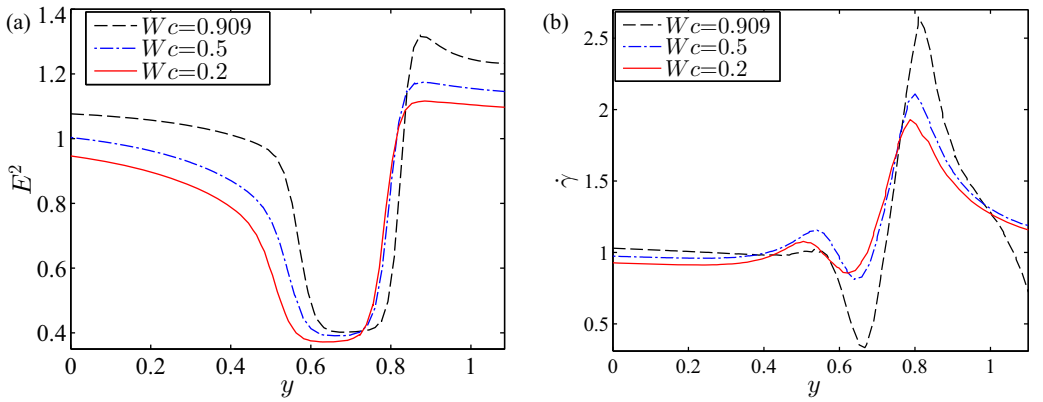

FIG. 15. Variation of (a) E^2 and (b) shear rate with the vertical distance at the tip of the droplet ($x = 2.11$) for a LD-LD system with $(R, S) = (0.5, 2)$. Other parameters are $\mathrm{Re} = 0.01$, $\lambda = 1$, and $M = 1$.

that reason, the value of steady state deformation decreases with increase in M and steady state configuration has been reached quickly.

D. Domain confinement-induced alteration in droplet breakup phenomenon

Figures 14(a) and 14(b) illustrate the influence of domain confinement on the droplet breakup mechanism for the PD-PD system with $S = 15$ and the LD-LD system with $(R, S) = (0.5, 2)$, respectively. In the absence of an electric field, the study of Sibillo *et al.* [22] has revealed that the breakup phenomenon of a droplet is suppressed in a highly confined domain. However, the present analysis shows a completely reversed phenomenon in the presence of an electric field. In the presence of an electric field, a LD droplet achieves steady state configuration in an unbounded domain ($\mathrm{Wc} = 0.2$) at $\mathrm{Ca}_E = 0.6$ and it undergoes sudden elongation in a confined domain ($\mathrm{Wc} = 0.909$) for the same value of Ca_E that ultimately leads the droplet to pinch off into daughter droplets. A similar phenomenon is also observed for a PD droplet, where it achieves steady state configuration in an unbounded domain at $\mathrm{Ca}_E = 0.90$. On the other hand, it undergoes breakup in a confined domain for the same value of Ca_E.

A proper physical explanation of the observed behavior is now provided. For a PD-PD system, the normal electric stress tries to deform the droplet toward the electrode whereas the viscous stress tries to resist its effect via deforming the droplet along the flow direction. For a PD-PD system, the magnitude of normal electric stress is high due to a higher value of S ($S = 15$). Furthermore, domain confinement again strengthens its value, which finally leads the droplet to undergo the breakup phenomenon. The reason behind the deformation phenomenon observed in Fig. 14(b) is slightly different. For the present LD-LD system, both the normal electric stress and normal hydrodynamic stress attempt to deform the droplet into an oblate shape in an unbounded domain. This is due to the negative value of the deformation characteristic function that is on the side of creating the oblate deformation. Likely, the viscous stress also tries to deform the droplet along the flow direction. However, as the effect of domain confinement on the governing stresses is not pronounced, it creates lower deformation and the droplet can succeed in achieving steady state configuration. However, in a confined domain, the scenario is changed a lot. For the selected values of (R, S), the electric field strength in the confined domain is very high as shown in Fig. 15(a). This necessarily stands for higher normal electric stress (as normal electric stress is proportional to E^2). Furthermore, the shear rate is also significantly high as shown in Fig. 15(b) which means the magnitude of viscous stress is also high in the confined domain. Although the reversed hydrodynamic stress tries to reduce the deformation in the confined domain, the droplet breaks up due to the integrated strength of normal electric stress and viscous stress.

Next, we discuss the effect of Ca_E (or electric field strength) on the breakup mechanism of the droplet in the confined domain. Figure 16 shows the transient evolution of the droplet shape for the LD-LD system with $(R, S) = (2, 0.5)$. The figure shows that, in the absence of an electric field, the breakup of the droplet occurs from midpoint, termed "midpoint pinching" and it produces three small and two large droplets. In the presence of moderate electric field strength, the number of daughter droplets produced increases, but the breakup mode remains unaltered. However, the most surprising aspect of droplet breakup dynamics is unveiled at higher electric field strength ($\mathrm{Ca}_E = 16$), where the breakup mode transforms from midpoint pinching to edge pinching. In the edge pinching mode, the droplets undergo breakup from their edges. This phenomenon is caused due to the cumulative effect of normal electric stress, hydrodynamic stress, and viscous stress in a confined domain. In the absence of an electric field, only viscous stress is present. This viscous stress stretches the droplet toward the flow direction and creates interfacial instability at the midsection of the droplet which leads the droplet to split into daughter droplets. In the presence of an electric field, normal electric stress and normal hydrodynamic stress also act in addition to viscous stress. For the considered values of (R, S), normal hydrodynamic stress acts in the direction of viscous stress, whereas normal electric stress acts toward the electrode. At moderate strength of electric field ($\mathrm{Ca}_E = 1.6$), the combined strength of normal hydrodynamic stress and viscous stress is dominating which speeds up the breakup phenomenon, creating interfacial instability at the midpoint of the droplet. However, at higher electric field, the strength of the normal electric stress increases, which attempts to stretch the droplets toward the electrode, whereas

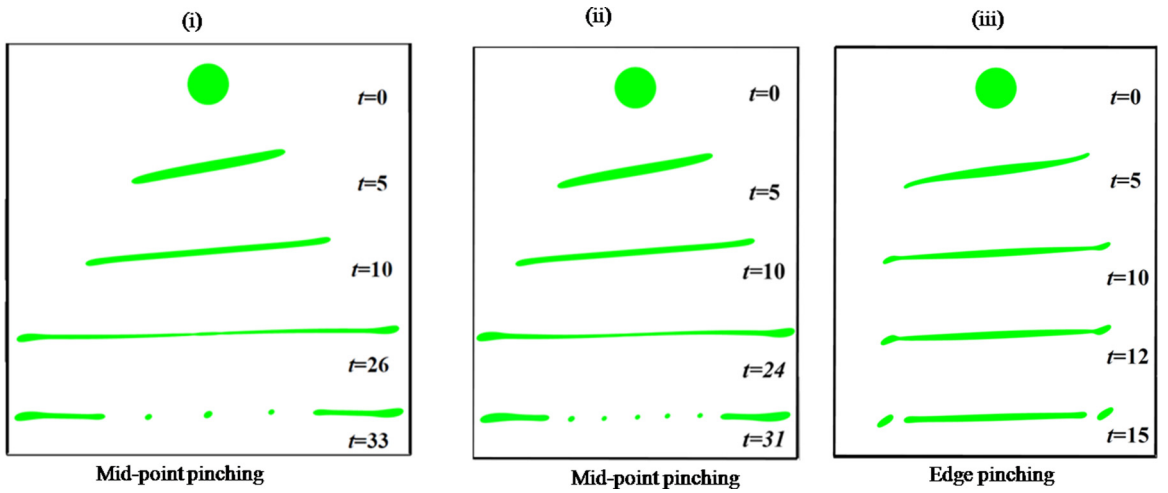

FIG. 16. Transient evolution of droplet shape for (i) $Ca_E = 0$, (ii) $Ca_E = 1.6$, and (iii) $Ca_E = 16$ for a LD-LD system with $(R, S) = (2, 0.5)$. Other parameters are $Re = 0.01$, $\lambda = 1$, $Ca = 1.6$, and $Wc = 0.55$.

viscous stress and normal hydrodynamic stress try to elongate it toward the flow direction. Because of this interplay among these forces, an interfacial mechanical instability is created at the droplet's edge and finally the daughter droplets are produced from the edges of the droplets keeping the central region intact.

Next, we have performed a large number of simulations for constructing a regime diagram defined by Ca_E and Wc as shown in Fig. 17. In the regime diagram, the blue-colored circular marker points shows the values of (Ca_E, Wc), at which no breakup is observed. On the other hand, the red-colored diamond marker points denote the values of (Ca_E, Wc), at which the droplet experiences breakup. From the regime diagram, it is also worth noting that the critical electric capillary number, at which breakup takes place, first increases

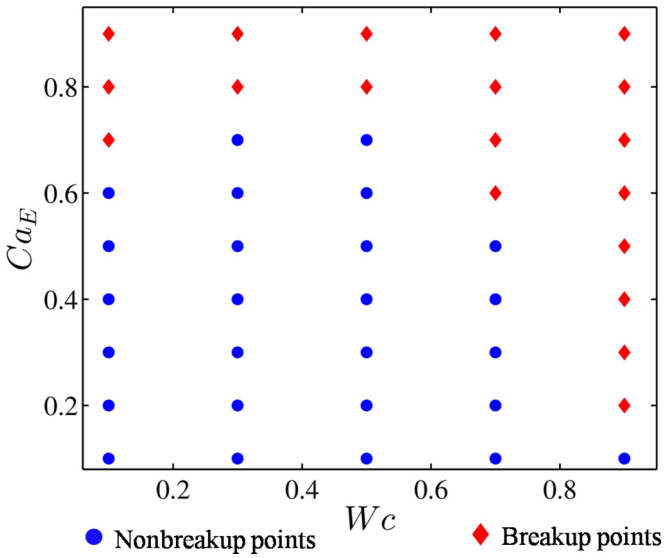

FIG. 17. Regime diagram of breakup and nonbreakup mode in Ca_E versus Wc space. Other parameters are $Re = 0.01$, $\lambda = 1$, $Ca = 0.6$, $S = 2$, and $R = 0.5$.

with domain confinement up to $Wc \approx 0.5$ and then decreases. This happens due to the variation of normal electric stress, normal hydrodynamic stress, and viscous stress with the degree of domain confinement.

E. Remarks on 2D analysis and its 3D counterparts

One major simplification of our current model is that the computations are restricted to two-dimensional analysis. Due to this limitation, an exact matching between the numerical results and experimental results is very hard to achieve. However, the 2D numerical analysis can give a good prediction of the phenomenon studied in a realistic microfluidic setup (Couette flow system), where the third dimension (which is perpendicular to the plane of velocity gradient and flow direction) is large enough to ignore any effect of the boundary on fluid flow and deformation dynamics. In this regard, it is worth mentioning that several researchers [20,21,34,49–55,38,56–59] have used the 2D numerical model in their analysis for capturing the essential physics related to the dynamics of the droplet in a realistic microfluidics setup. For example, Stan *et al.* have studied the droplet migration characteristics in a pressure-driven flow and found that the numerical simulation results in the 2D domain are very similar to the 3D domain, and both results compare well with the experiments [53]. Furthermore, we can directly use the present numerical result for a confined liquid column in a real microfluidic setup subjected to the combined presence of background shear flow and transverse electric field [60–63]. It is worth mentioning that, in the sole presence of background shear flow, several similarities exist between the 2D and 3D dynamics of the droplet, like the creation of the regions of high interfacial curvature, tip streaming, formation of reentrant cavities because of the local pressure gradient, and migration of the droplet toward the region of minimal shear. There are also several similarities between the 2D and 3D elctrohydrodynamics (EHD) of the droplets. In the sole presence of a uniform electric field, the electric-field-induced fluid flow (EHD flow) in a plane which is perpendicular to the equator of the droplet and parallel to the direction of electric

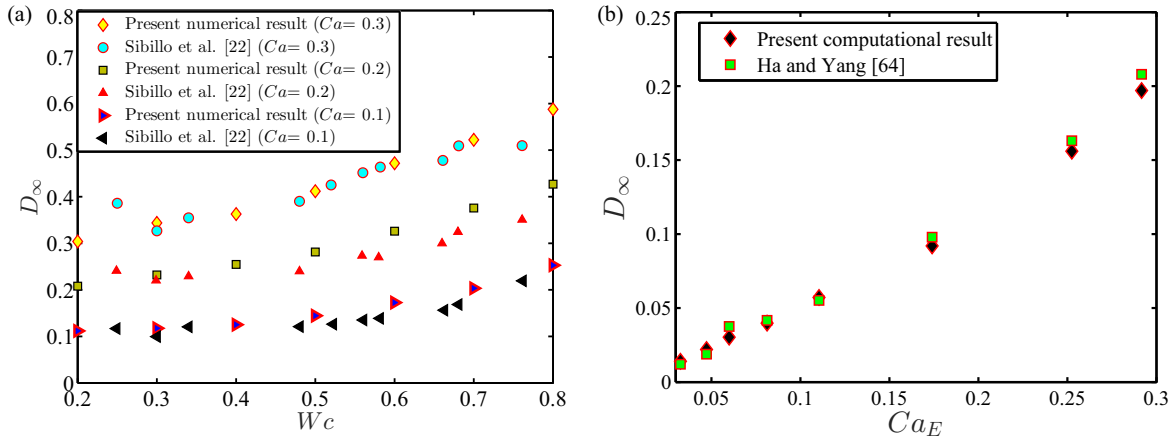

FIG. 18. (a) Variation of steady state deformation parameter with domain confinement for different values of Ca. Other parameters are values are $\lambda = 1$ and $\mathrm{Re} = 0.05$. (b) Variation of steady state deformation parameter with electric capillary number. Other properties are $R = 10$, $S = 1.37$, $\lambda = 0.874$, and $\mathrm{Re} = 0.01$.

field are exactly identical for 2D and 3D droplets. For both the 2D and 3D cases, the EHD flow contains four circulation rolls in the inside region of the droplet, which are again matched by their counterparts in the suspending fluid.

Another important thing is that the direction of the EHD flow is exactly same for both the 2D and 3D droplets; the EHD flow is directed from equators to poles for $R > S$ and poles to equators for $S > R$, where R and S denotes the ratios of conductivity (σ) and permittivity (ε) of the droplet and the carrier fluid. In this regard, we have made a comparison between our 2D numerical result with the experimental results of Sibillo *et al.* [22] as well as Ha and Yang [64] as depicted in Figs. 18(a) and 18(b), respectively. Therefore, there is enough reason to expect that the current two-dimensional computational results will provide ample realistic insight into the deformation characteristic of the droplet in a realistic microfluidic setup and it will maintain a notable degree of physical significance.

IV. CONCLUSIONS

We have analyzed the interplay of electromechanics and hydrodynamics toward dictating the morphodynamic evolution of a droplet in a confined shear flow. The key findings from our study are summarized below.

(i) The presence of a transverse electric field significantly alters the monotonic variation of the droplet deformation parameter with confinement ratio. For both the PD-PD and LD-LD systems, we have obtained nonmonotonic variation of droplet deformation parameter with the domain confinement.

(ii) In a highly confined domain, for both types of PD-PD systems ($S > 1$ and $S < 1$), the steady state deformation reduces with increases in the electric field strength. On the other hand, for the PD-PD system having $S > 1$, the presence of an electric field amplifies the oscillatory dynamics. Therefore, the droplet achieves steady state configuration very sluggishly. On the contrary, for the $S < 1$ case, the oscillation diminishes with increase in the electric field strength and the droplet achieves steady state configuration very quickly.

(iii) In a highly confined domain, the value of the steady state deformation parameter increases with electric field strength for the LD-LD system having $\Phi < 0$. For this system, the unsteadiness in the deformation and orientation of the droplet also increases with the increase in electric field strength. Hence, the droplet attains steady state configuration very slowly. On the contrary, the magnitude of deformation parameter as well as the oscillation in the deformation and orientation of the droplet decrease with the enhancement of electric field strength for the LD-LD system having $\Phi > 0$.

(iv) For both the PD-PD system having $S > 1$ and the LD-LD system having $\Phi < 0$, the higher domain confinement incites the droplet breakup phenomenon under electrohydrodynamic interactions. Another interesting fact is that, with the augmentation of electric field strength in the confined domain, the droplet breakup mode transforms from the midpoint pinching mode to the edge pinching mode for a LD-LD system having $\Phi > 0$.

(v) For a LD-LD system having $\Phi < 0$, the critical electric capillary number shows a nonmonotonic dependence on the channel confinement.

ACKNOWLEDGMENT

S.C. acknowledges the financial support provided by the Department of Science and Technology, Government of India, through the J. C. Bose National Fellowship, for executing this research.

APPENDIX A: ANALYTICAL SOLUTION FOR THE EHD OF DROPLET IN UNCONFINED DOMAIN

Neglecting the influence of wall confinement, an analytical solution for the present EHD problem has been developed under the Stokes flow condition. In an unconfined domain, at a lower value of Ca, the strength of the hydrodynamic stress is low, which creates small deformation. Due to that, the droplet shape deviates insignificantly from its spherical nature. Again, $M \sim 1$ implicates that the electric stress is also less. This means that the deformation due to electric-field-induced electric stress is also less, which allows us to obtain an analytical solution of electric potential and velocity field by using the regular perturbation method taking Ca_E

or Ca as a perturbation variable. Here, we have considered Ca as a perturbation parameter for the sake of convenience. In the regular perturbation method, the expansion of each dependent variable takes the following perturbation form [44,45]:

$$\chi = \chi^{(0)} + \mathrm{Ca}\chi^{(\mathrm{Ca})} + \mathrm{Ca}^2\chi^{(\mathrm{Ca}^2)} + O(\mathrm{Ca}^3), \tag{A1}$$

where $\chi^{(0)}$ depicts the leading-order term of χ without shape deformation and $\chi^{(\mathrm{Ca})}$ shows the correction term with the shape deformation.

For an electrostatic problem, the electric potential should satisfy the Laplace equation. The electric potential inner and outer side of the droplet can be expressed in the following form:

$$\phi_i = \sum_{n=1}^{\infty} r^n \sum_{m=1}^{n} [a_{n,m}\cos(m\theta) + \hat{a}_{n,m}\sin(m\theta)], \tag{A2}$$

$$\phi_e = -\mathbf{E}_\infty \cdot \mathbf{r} + \sum_{n=1}^{\infty} \frac{1}{r^n} \sum_{m=1}^{n} [b_{n,m}\cos(m\phi) + \hat{b}_{n,m}\sin(m\phi)]. \tag{A3}$$

The unknown coefficients at each order of perturbation are obtained by applying the appropriate boundary condition at the droplet interface (continuity of electric potential and normal current density).

Under the Stokes flow condition, we can express the flow field solely in terms of a fourth-order biharmonic equation for the stream function. General solution of the stream function for the inner and outer phases of the droplet can be expressed in the following form:

$$\psi_i = \sum_{n=2}^{\infty} r^n \sum_{m=2}^{n} [A_{n,m}\cos(m\theta) + \hat{A}_{n,m}\sin(m\theta) + B_{n,m}(t)r^2\cos(m\theta) + \hat{B}_{n,m}(t)r^2\sin(m\theta)], \tag{A4}$$

$$\psi_e = \left(\frac{r^2}{4}\right) - \left[\frac{r^2}{4}\cos(2\theta)\right] + \sum_{n=2}^{\infty} r^{-n} \sum_{m=2}^{n} \begin{bmatrix} C_{n,m}\cos(m\theta) + \hat{C}_{n,m}\sin(m\theta) \\ +E_{n,m}r^2\cos(m\theta) + \hat{E}_{n,m}r^2\sin(m\theta) \end{bmatrix}. \tag{A5}$$

Here also, we have calculated the unknown coefficient of Eqs. (A4) and (A5) by using the appropriate interfacial boundary condition (no-slip and no-penetration boundary condition of the velocity and tangential stress boundary condition). By applying the normal stress boundary condition, we have calculated the droplet shape. This eventually leads to the expressions of various terms in Eq. (17) in the following form:

$$\begin{aligned}
L^{(\mathrm{Ca})}{}_{2,0} &= -\frac{M(R^2+R-3S+1)}{3(R+1)^2}\left[1-\exp\left(-\frac{t}{\lambda+1}\right)\right],\\
\hat{L}^{(\mathrm{Ca})}_{2,0} &= 1-\exp\left(-\frac{t}{\lambda+1}\right),\\
L^{(\mathrm{Ca}^2)}{}_{0,1} &= -\frac{1}{4}(L_{2,0})^2 - \frac{1}{4}(\hat{L}_{2,0})^2,\\
L^{(\mathrm{Ca}^2)}{}_{2,1} &= -\frac{M(R-1)(R^2+R-3S+1)\{l_1+l_2+l_3\}}{72(1+R)^5}\exp\left(-\frac{t}{\lambda+5}\right),\\
\hat{L}^{(\mathrm{Ca}^2)}_{2,1} &= \frac{M(R-1)\{\hat{l}_1+\hat{l}_2+\hat{l}_3\}}{24(R+1)^3}\exp\left(-\frac{t}{\lambda+5}\right),\\
L^{(\mathrm{Ca}^2)}{}_{4,1} &= \frac{\{k_1+k_2+k_3+k_4\}}{720(5\lambda+13)(1+\lambda)(\lambda+2)(1+R^4)}\exp\left(-\frac{6t}{11\lambda+19}\right),\\
\hat{L}^{(\mathrm{Ca}^2)}_{4,1} &= -\frac{M\{\hat{k}_1+\hat{k}_2+\hat{k}_3+\hat{k}_4\}}{360(\lambda+2)(5\lambda+13)(\lambda+1)(R+1)^2}\exp\left(-\frac{6t}{11\lambda+19}\right),
\end{aligned} \tag{A6}$$

where

$$\begin{aligned}
l_1 &= (R^2\lambda+13R^2-2R\lambda-12S\lambda+38R-28S+\lambda+13)\exp\left[-\frac{4t}{(\lambda+1)(\lambda+5)}\right],\\
l_2 &= \frac{4(R^2\lambda+13R^2-2R\lambda-12S\lambda+38R-28S+\lambda+13)}{1+\lambda}\exp\left[\frac{t}{(\lambda+5)}\right],\\
l_3 &= -\frac{(\lambda+5)(R^2\lambda+13R^2-2R\lambda-12S\lambda+38R-28S+\lambda+13)}{1+\lambda},
\end{aligned} \tag{A7}$$

$$\begin{aligned}
\hat{l}_1 &= (R^2\lambda+13R^2-2R\lambda-12S\lambda+38R-28S+\lambda+13)\exp\left[-\frac{4t}{(\lambda+5)(\lambda+1)}\right],\\
\hat{l}_2 &= \frac{4(R^2\lambda+13R^2-2R\lambda-12S\lambda+38R-28S+\lambda+13)}{\lambda+1}\exp\left(\frac{t}{\lambda+5}\right),\\
\hat{l}_3 &= -\frac{(R^2\lambda+13R^2-2R\lambda-12S\lambda+38R-28S+\lambda+13)(\lambda+5)}{\lambda+1},
\end{aligned} \tag{A8}$$

$$
k_1 = \begin{pmatrix} 700M^2R^4\lambda^3 + 4400M^2R^4\lambda^2 + 1200M^2R^3\lambda^3 - 4000M^2R^2S\lambda^3 \\ +9068M^2R^4\lambda + 7040M^2R^3\lambda^2 - 24640M^2R^2S\lambda^2 + 1900M^2R^2\lambda^3 \\ -3400M^2RS\lambda^3 + 5700M^2S^2\lambda^3 - 6180R^4\lambda^3 + 6136M^2R^4 \\ +13232M^2R^3\lambda - 49504M^2R^2S\lambda + 11440M^2R^2\lambda^2 - 19360M^2RS\lambda^2 \\ +1200M^2R\lambda^3 + 34320M^2S^2\lambda^2 - 4000M^2S\lambda^3 - 37008R^4\lambda^2 - 24720R^3\lambda^3 \\ +7904M^2R^3 - 32448M^2R^2S + 22300M^2R^2\lambda - 34792M^2RS\lambda + 7040M^2R\lambda^2 \\ +66900M^2S^2\lambda - 24640M^2S\lambda^2 + 700M^2\lambda^3 - 71604R^4\lambda - 148032R^3\lambda^2 - \\ 37080R^2\lambda^3 + 14040M^2R^2 - 19344M^2RS + 13232M^2R\lambda + 42120M^2S^2 \\ -49504M^2S\lambda + 4400M^2\lambda^2 - 44616R^4 - 286416R^3\lambda - 222048R^2\lambda^2 \\ -24720R\lambda^3 + 7904M^2R - 32448M^2S + 9068M^2\lambda - 178464R^3 - 429624R^2\lambda \\ -148032R\lambda^2 - 6180\lambda^3 + 6136M^2 - 267696R^2 - 286416R\lambda - 37008\lambda^2 \\ -178464R - 71604\lambda - 44616 \end{pmatrix} \exp\left[-\frac{6t}{(11\lambda+19)}\right]
$$

$$
k_2 = \begin{pmatrix} 175M^2R^4\lambda^3 + 965M^2R^4\lambda^2 + 350M^2R^3\lambda^3 - 1050M^2R^2S\lambda^3 \\ +1661M^2R^4\lambda + 1930M^2R^3\lambda^2 - 5790M^2R^2S\lambda^2 + 525M^2R^2\lambda^3 \\ -1050M^2RS\lambda^3 + 1575M^2S^2\lambda^3 - 1575R^4\lambda^3 + 871M^2R^4 \\ +3322M^2R^3\lambda - 9966M^2R^2S\lambda + 2895M^2R^2\lambda^2 - 5790M^2RS\lambda^2 \\ +350M^2R\lambda^3 + 8685M^2S^2\lambda^2 - 1050M^2S\lambda^3 - 8685R^4\lambda^2 \\ -6300R^3\lambda^3 + 1742M^2R^3 - 5226M^2R^2S + 4983M^2R^2\lambda \\ -9966M^2RS\lambda + 1930M^2R\lambda^2 + 14949M^2S^2\lambda - 5790M^2S\lambda^2 \\ +175M^2\lambda^3 - 14949R^4\lambda - 34740R^3\lambda^2 - 9450R^2\lambda^3 + 2613M^2R^2 \\ -5226M^2RS + 3322M^2R\lambda + 7839M^2S^2 - 9966M^2S\lambda \\ +965M^2\lambda^2 - 7839R^4 - 59796R^3\lambda - 52110R^2\lambda^2 - 6300R\lambda^3 \\ +1742M^2R - 5226M^2S + 1661M^2\lambda - 31356R^3 - 89694R^2\lambda \\ -34740R\lambda^2 - 1575\lambda^3 + 871M^2 - 47034R^2 - 59796R\lambda - 8685\lambda^2 \\ -31356R - 14949\lambda - 7839 \end{pmatrix} \exp\left(-\left[\frac{16t(\lambda+2)}{(11\lambda+9)(\lambda+1)}\right]\right)
$$

$$
k_3 = \begin{pmatrix} 280M^2R^4\lambda^3 + 1184M^2R^4\lambda^2 + 320M^2R^3\lambda^3 - 1440M^2R^2S\lambda^3 \\ +1592M^2R^4\lambda + 640M^2R^3\lambda^2 - 5376M^2R^2S\lambda^2 + 600M^2R^2\lambda^3 \\ -720M^2RS\lambda^3 + 1800M^2S^2\lambda^3 - 2376R^4\lambda^3 + 688M^2R^4 - 320M^2R^3\lambda \\ -6048M^2R^2S\lambda + 1824M^2R^2\lambda^2 - 192M^2RS\lambda^2 + 320M^2R\lambda^3 \\ +5472M^2S^2\lambda^2 - 1440M^2S\lambda^3 - 7776R^4\lambda^2 - 9504R^3\lambda^3 - 640M^2R^3 \\ -2112^*M^2R^2S + 1272M^2R^2\lambda + 4464M^2RS\lambda + 640M^2R\lambda^2 \\ +3816M^2S^2\lambda - 5376M^2S\lambda^2 + 280M^2\lambda^3 - 6696R^4\lambda - 31104R^3\lambda^2 \\ -14256R^2\lambda^3 + 48M^2R^2 + 3936M^2RS - 320M^2R\lambda + 144M^2S^2 \\ -6048M^2S\lambda + 1184M^2\lambda^2 - 1296R^4 - 26784R^3\lambda - 46656R^2\lambda^2 \\ -9504R\lambda^3 - 640M^2R - 2112M^2S + 1592M^2\lambda - 5184R^3 \\ -40176R^2\lambda - 31104R\lambda^2 - 2376\lambda^3 + 688M^2 - 7776R^2 \\ -26784R\lambda - 7776\lambda^2 - 5184R - 6696\lambda - 1296 \end{pmatrix} \exp\left(-\left[\frac{t(5\lambda+13)}{(11\lambda+9)(\lambda+1)}\right]\right)
$$

$$
k_4 = \begin{pmatrix} -1155M^2R^4\lambda^3 - 6549M^2R^4\lambda^2 - 1870M^2R^3\lambda^3 + 6490M^2R^2S\lambda^3 - 12321M^2R^4\lambda \\ -9610M^2R^3\lambda^2 + 35806M^2R^2S\lambda^2 - 3025M^2R^2\lambda^3 + 5170M^2RS\lambda^3 - 9075M^2S^2\lambda^3 \\ +10131R^4\lambda^3 - 7695M^2R^4 - 16234M^2R^3\lambda + 65518M^2R^2S\lambda - 16159M^2R^2\lambda^2 \\ +25342M^2RS\lambda^2 - 1870M^2R\lambda^3 - 48477M^2S^2\lambda^2 + 6490M^2S\lambda^3 + 53469R^4\lambda^2 \\ +40524R^3\lambda^3 - 9006M^2R^3 + 39786M^2R^2S - 28555M^2R^2\lambda + 40294M^2RS\lambda \\ -9610M^2R\lambda^2 - 85665M^2S^2\lambda + 35806M^2S\lambda^2 - 1155M^2\lambda^3 + 93249R^4\lambda + 213876R^3\lambda^2 \\ +60786R^2\lambda^3 - 16701M^2R^2 + 20634M^2RS - 16234M^2R\lambda - 50103M^2S^2 + 65518M^2S\lambda \\ -6549M^2\lambda^2 + 53751R^4 + 372996R^3\lambda + 320814R^2\lambda^2 + 40524R\lambda^3 - 9006M^2R \\ +39786M^2S - 12321M^2\lambda + 215004R^3 + 559494R^2\lambda + 213876R\lambda^2 + 10131\lambda^3 \\ -7695M^2 + 322506R^2 + 372996R\lambda + 53469\lambda^2 + 215004R + 93249\lambda + 53751 \end{pmatrix}, \tag{A9}
$$

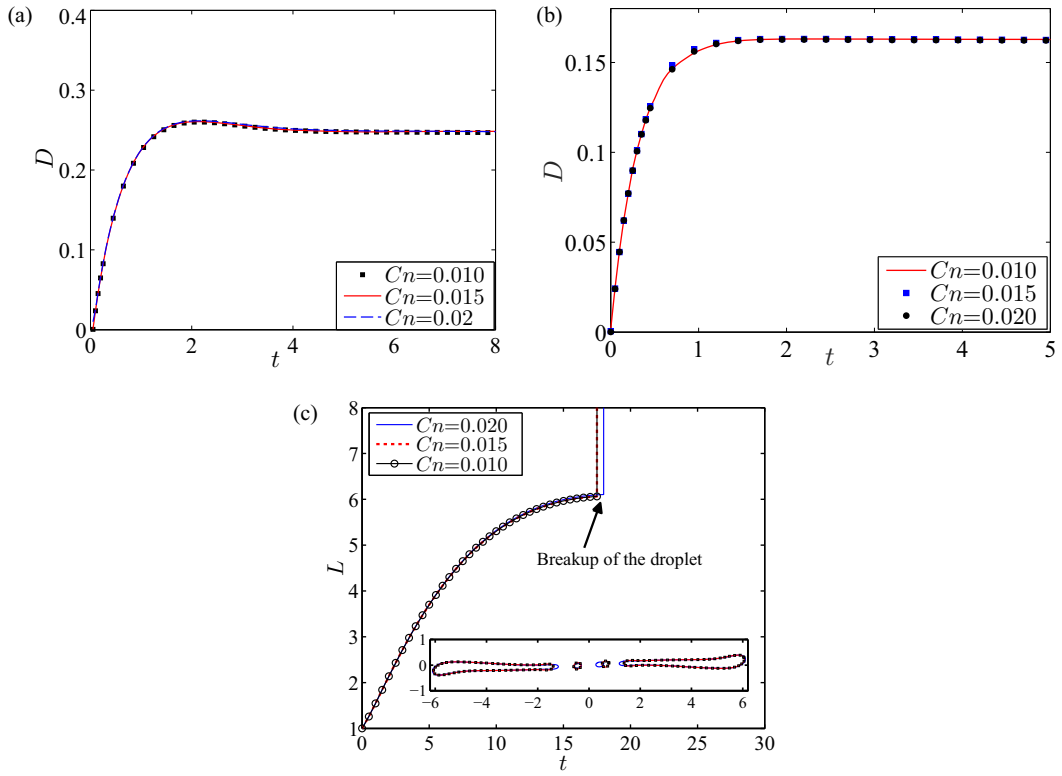

FIG. 19. Grid and Cn independence study. Deformation of the droplet interface in (a) simple shear flow with Ca = 0.1, Wc = 0.8; (b) shear flow with electric field having $S = 15$, Ca = 0.14, $M = 1$, Wc = 0.2. (c) Breakup dynamics of the droplet in the combined presence of shear flow and electric field. Other parameters are Re = 0.01, Wc = 0.9, $\lambda = 1$, Ca = 0.6, $S = 2$, $R = 0.5$, and $\mathrm{Ca}_E = 0.4$.

$$\hat{k}_1 = \begin{pmatrix} 2080R^2\lambda^3 + 12768R^2\lambda^2 + 1780R\lambda^3 - 5940S\lambda^3 + 25536R^2\lambda \\ +10128R\lambda^2 - 35664S\lambda^2 + 2080\lambda^3 + 16640R^2 + 18180R\lambda \\ -69252S\lambda + 12768\lambda^2 + 10088R - 43368S + 25536\lambda + 16640 \end{pmatrix} \exp\left(\frac{6t}{11\lambda + 9}\right),$$

$$\hat{k}_2 = \begin{pmatrix} 525R^2\lambda^3 + 2895R^2\lambda^2 + 525R\lambda^3 - 1575S\lambda^3 + 4983R^2\lambda + 2895R\lambda^2 \\ -8685S\lambda^2 + 525\lambda^3 + 2613R^2 + 4983R\lambda - 14949S\lambda + 2895\lambda^2 \\ +2613R - 7839S + 4983\lambda + 2613 \end{pmatrix} \exp\left[-\frac{16t(\lambda + 2)}{(11\lambda + 9)(\lambda + 1)}\right],$$

$$\hat{k}_3 = \begin{pmatrix} 816R^2\lambda^3 + 3072R^2\lambda^2 + 456R\lambda^3 - 2088S\lambda^3 + 3504R^2\lambda \\ +480R\lambda^2 - 6624S\lambda^2 + 816\lambda^3 + 1248R^2 - 1752R\lambda - 5256S\lambda \\ +3072\lambda^2 - 1776R - 720S + 3504\lambda + 1248 \end{pmatrix} \exp\left[-\frac{t(5\lambda + 13)}{(11\lambda + 9)(\lambda + 1)}\right],$$

$$\hat{k}_4 = \begin{pmatrix} -3421R^2\lambda^3 - 18735R^2\lambda^2 - 2761R\lambda^3 + 9603S\lambda^3 - 34023R^2\lambda \\ -13503R\lambda^2 + 50973S\lambda^2 - 3421\lambda^3 - 20501R^2 - 21411R\lambda + 89457S\lambda \\ -18735\lambda^2 - 10925R + 51927S - 34023\lambda - 20501 \end{pmatrix}. \tag{A10}$$

APPENDIX B: GRID AND CAHN NUMBER INDEPENDENCE STUDY

For assuring the correctness of the numerical simulation, grid and Cn number independence studies are required. As grid size and Cn number are equal near the interface, a correct Cn independence study automatically satisfies a correct grid size independence study [65].

For performing the Cn independence test, the deformation parameter (D) has been evaluated for two cases: (a) The droplet is suspended in a simple shear flow with Wc = 0.80, Ca = 0.1, and Re = 0.01, and (b) the droplet is suspended in simple shear flow under a transverse electric field with Wc = 0.20, Ca = 0.14, $M = 1$, and Re = 0.01 as shown in Figs. 19(a) and 19(b), respectively. For both cases, we have considered three different Cahn numbers (Cn = 0.02, 0.01, 0.015). From the figures, a negligible variation in deformation characteristic is observed for the selected Cn numbers. It is also worth mentioning that the droplet breakup dynamics is more sensitive to the spatial resolution. For confirming that the droplet breakup dynamics is independent of the spatial resolution, we have also performed a grid independence study

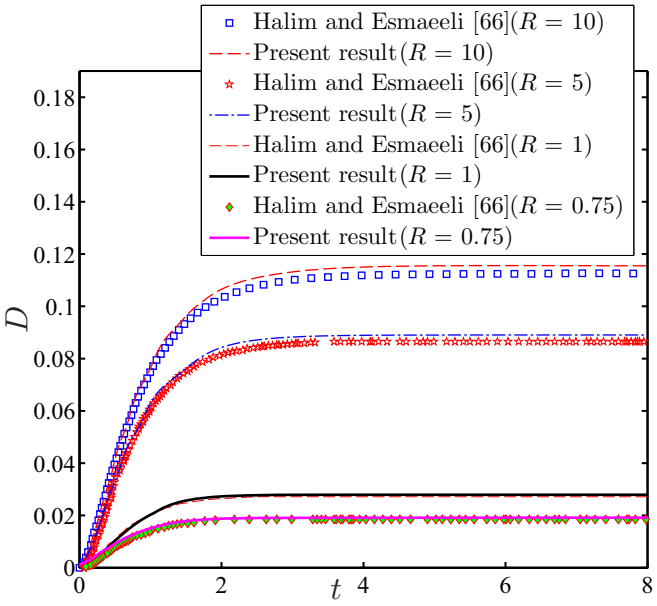

FIG. 20. Comparison of present simulation result and the numerical results of Halim and Esmaeeli [66].The parameters considered are $S = 0.5$, $\lambda = 1$, Re $= 1$, $\bar{\rho} = 0.5$, $M = 1$, and $\mathrm{Ca}_E = 0.25$.

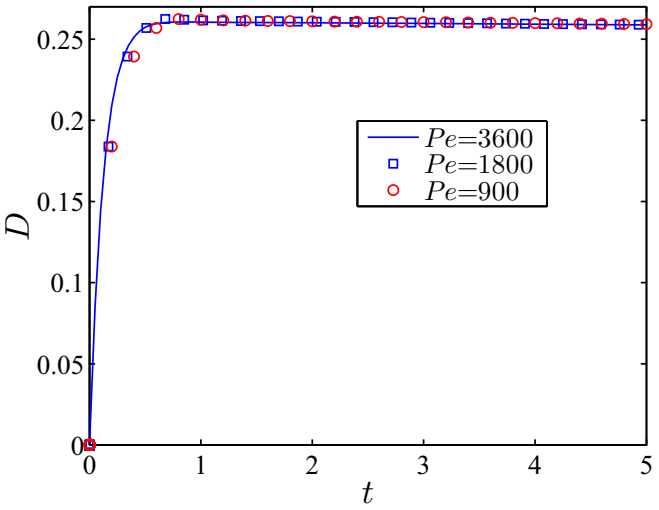

FIG. 21. Transient variation of deformation parameter for different values of Pe. Other parameters are Ca $= 0.1$, $M = 10$, $R = 2$, $S = 0.5$, Cn $= 0.01$, $\lambda = 1$, and Re $= 0.01$.

(or Cahn number independence study) in Fig. 19(c). This figure demonstrates that the breakup dynamics of the droplet becomes independent of Cn below Cn $= 0.015$. Therefore, we have chosen Cn $= 0.015$ for studying the deformation dynamics as well as breakup dynamics of the droplet. In our present study, all the figures obtained from numerical data have been plotted for Cn $= 0.015$.

APPENDIX C: MODEL VALIDATION STUDY

In this section, we have validated our 2D numerical result with the experimental result of Sibillo *et al.* [22] as shown in Fig. 18(a), where a liquid droplet is suspended in another liquid medium under confined shear flow condition. This study clearly shows good matching between the numerical and experimental result. Furthermore, we have performed another comparison of our numerical result with the experimental result of Ha and Yang [64] as shown in Fig. 18(b), where the droplet is subjected to a uniform transverse electric field. This comparison also shows good qualitative matching between our numerical result and the experimental results of Ha and Yang [64], where the magnitude of deformation increases with the enhancement of Ca_E for both the numerical and experimental observations. Furthermore, we have compared our numerical results with the numerical results of Halim and Esmaeeli [66] for a relatively higher value of Ca_E, where we have shown the transient evolution of the deformation of the droplet under a uniform electric field for different values of electrical conductivity as shown in Fig. 20. This figure shows very good agreement between our numerical results and the results of Halim and Esmaeeli [66].

APPENDIX D: PÉCLET NUMBER INDEPENDENCE STUDY

In phase field formalism, the Péclet number denotes the ratio convective and diffusive transport of the phase field order parameter. In phase field method, we have used a diffused interface for tracking the fluid-fluid interface implicitly. Therefore, the simulated results should be independent of the Péclet number [67]. In order to ensure that, we have performed a Péclet number independence study as shown in Fig. 21 and we have found a negligible variation in the obtained results for the considered values of the Péclet number. Finally, we have used Pe $= 1800$ for the present numerical analysis [43].

[1] H. A. Stone, A. D. Stroock, and A. Ajdari, Annu. Rev. Fluid Mech. **36**, 381 (2004).
[2] J. S. Eow and M. Ghadiri, Colloids Surf. A **219**, 253 (2003).
[3] S. Mhatre, V. Vivacqua, M. Ghadiri, A. M. Abdullah, A. Hassanpour, B. Hewakandamby, B. Azzopardi, and B. Kermani, Chem. Eng. Res. Des. **96**, 177 (2015).
[4] K. J. Ptasinski and P. J. A. M. Kerkhof, Sep. Sci. Technol. **27**, 995 (1992).
[5] S. Santra, S. Das, S. S. Das, and S. Chakraborty, Microfluid. Nanofluid. **22**, 88 (2018).
[6] K. Ahn, C. Kerbage, T. P. Hunt, R. M. Westervelt, D. R. Link, and D. A. Weitz, Appl. Phys. Lett. **88**, 024104 (2006).
[7] D. R. Link, E. Grasland-Mongrain, A. Duri, F. Sarrazin, Z. Cheng, G. Cristobal, M. Marquez, and D. A. Weitz, Angew. Chem. **45**, 2556 (2006).
[8] J. D. Wehking and R. Kumar, Lab Chip **15**, 793 (2015).
[9] V. Cristini and Y.-C. Tan, Lab Chip **4**, 257 (2004).
[10] G. I. Taylor, Proc. R. Soc. London, Ser. A **146**, 501 (1934).
[11] A. M. Ardekani, S. Dabiri, and R. H. Rangel, Phys. Fluids **21**, 093302 (2009).

[12] H. D. Ceniceros, R. L. Nós, and A. M. Roma, J. Comput. Phys. **229**, 6135 (2010).
[13] C. E. Chaffey and H. Brenner, J. Colloid Interface Sci. **24**, 258 (1967).
[14] J. M. Rallison, Annu. Rev. Fluid Mech. **16**, 45 (1984).
[15] H. A. Stone, Annu. Rev. Fluid Mech. **26**, 65 (1994).
[16] J. Gounley, G. Boedec, M. Jaeger, and M. Leonetti, J. Fluid Mech. **791**, 464 (2016).
[17] N. Wang, H. Liu, and C. Zhang, J. Rheol. (NY, USA) **61**, 741 (2017).
[18] H. Liu, Y. Ba, L. Wu, Z. Li, G. Xi, and Y. Zhang, J. Fluid Mech. **837**, 381 (2018).
[19] Y. Ba, N. Wang, H. Liu, Q. Li, and G. He, Phys. Rev. E **97**, 033307 (2018).
[20] N. Barai and N. Mandal, Phys. Fluids **28**, 073302 (2016).
[21] S. Santra, S. Mandal, and S. Chakraborty, Phys. Fluids **30**, 062003 (2018).
[22] V. Sibillo, G. Pasquariello, M. Simeone, V. Cristini, and S. Guido, Phys. Rev. Lett. **97**, 054502 (2006).
[23] R. Cardinaels, S. Afkhami, Y. Renardy, and P. Moldenaers, J. Non-Newtonian Fluid Mech. **166**, 52 (2011).
[24] P. J. A. Janssen and P. D. Anderson, Phys. Fluids **19**, 043602 (2007).
[25] A. J. Griggs, A. Z. Zinchenko, and R. H. Davis, Int. J. Multiphase Flow **33**, 182 (2007).
[26] J. D. Wehking, L. Chew, and R. Kumar, Appl. Phys. Lett. **103**, 054101 (2013).
[27] A. R. Thiam, N. Bremond, and J. Bibette, Phys. Rev. Lett. **102**, 188304 (2009).
[28] S. Mandal, A. Bandopadhyay, and S. Chakraborty, Phys. Rev. E **93**, 043127 (2016).
[29] S. Mandal, A. Bandopadhyay, and S. Chakraborty, Phys. Fluids **28**, 062006 (2016).
[30] S. Mandal, K. Chaudhury, and S. Chakraborty, Phys. Rev. E **89**, 053020 (2014).
[31] A. Bandopadhyay, S. Mandal, N. K. Kishore, and S. Chakraborty, J. Fluid Mech. **792**, 553 (2017).
[32] S. Mandal, A. Bandopadhyay, and S. Chakraborty, J. Fluid Mech. **809**, 726 (2016).
[33] Y. Cui, N. Wang, and H. Liu, Phys. Fluids **31**, 022105 (2019).
[34] S. Santra, D. Sen, S. Das, and S. Chakraborty, Phys. Fluids **31**, 032005 (2019).
[35] C. T. O'Konski and H. C. Thacher, Jr., J. Phys. Chem. **57**, 955 (1953).
[36] G. I. Taylor, Proc. R. Soc. London, Ser. A **291**, 159 (1966).
[37] J. C. Baygents, N. J. Rivette, and H. A. Stone, J. Fluid Mech. **368**, 359(1998).
[38] S. Mahlmann and D. T. Papageorgiou, J. Fluid Mech. **626**, 367 (2009).
[39] E. Lac and G. M. Homsy, J. Fluid Mech. **590**, 239 (2007).
[40] S. Torza, R. G. Cox, and S. G. Mason, Philos. Trans. R. Soc. A **269**, 295 (1971).
[41] D. A. Saville, Annu. Rev. Fluid Mech. **29**, 27 (1997).
[42] Y. Lin, P. Skjetne, and A. Carlson, Int. J. Multiphase Flow **45**, 1 (2012).
[43] Q. Yang, B. Q. Li, and Y. Ding, Int. J. Multiphase Flow **57**, 1 (2013).
[44] S. Mandal and S. Chakraborty, Phys. Fluids **29**, 072109 (2017).
[45] S. Mandal and S. Chakraborty, Phys. Rev. Fluids **2**, 93602 (2017).
[46] T. Tsukada, T. Katayama, Y. Ito, and M. Hozawa, J. Chem. Eng. Jpn. **26**, 698 (1993).
[47] P. F. Salipante and P. M. Vlahovska, Phys. Fluids **22**, 112110 (2010).
[48] A. Behjatian and A. Esmaeeli, Int. J. Multiphase Flow **48**, 71 (2013).
[49] S. Mortazavi and G. Tryggvason, J. Fluid Mech. **411**, 325 (2000).
[50] M. Qiu, S. Afkhami, C.-Y. Chen, and J. J. Feng, J. Fluid Mech. **846**, 121 (2018).
[51] Q. Dong and A. Sau, Phys. Rev. Fluids **3**, 73701 (2018).
[52] R. Charles and C. Pozrikidis, J. Fluid Mech. **365**, 205 (1998).
[53] C. A. Stan, L. Guglielmini, A. K. Ellerbee, D. Caviezel, H. A. Stone, and G. M. Whitesides, Phys. Rev. E **84**, 036302 (2011).
[54] Y. Chen and C. Wang, Phys. Rev. E **90**, 033010 (2014).
[55] K. Chaudhury, S. Mandal, and S. Chakraborty, Phys. Rev. E **93**, 023106 (2016).
[56] H. Zhou and C. Pozrikidis, Phys. Fluids A **5**, 311 (1993).
[57] E. Yariv and I. Frankel, J. Fluid Mech. **788**, R2 (2016).
[58] Q. Dong and A. Sau, Phys. Rev. E **99**, 043106 (2019).
[59] S. Santra, S. Das, and S. Chakraborty, Phys. Fluids **31**, 062004 (2019).
[60] P. H. Rhodes, R. S. Snyder, and G. O. Roberts, J. Colloid Interface Sci. **129**, 78 (1989).
[61] L. Limat, H. A. Stone, and J. L. Viovy, Phys. Fluids **10**, 2439 (1998).
[62] M. Trau, S. Sankaran, D. A. Saville, and I. A. Aksay, Langmuir **11**, 4665 (1995).
[63] A. Esmaeeli, Phys. Fluids **28**, 073306 (2016).
[64] J.-W. Ha and S.-M. Yang, J. Fluid Mech. **405**, 131 (2000).
[65] S. Mandal, U. Ghosh, A. Bandopadhyay, and S. Chakraborty, J. Fluid Mech. **776**, 390 (2015).
[66] M. A. Halim and A. Esmaeeli, Fluid Dyn. Mater. Process. **9**, 435 (2013).
[67] P. Yue, J. J. Feng, C. Liu, and J. Shen, J. Fluid Mech. **515**, 293 (2004).